The closuring errors were distributed in relation to the horizontal distance. The altitudes of the stations were presented in Ap.II-1.

1-2-4 Corrections and Data Processing

For the first step of the data processing, gravity data as obtained in the field must be corrected for tide, height of instruments, drift, latitude, influence of topography, altitude, free-air, Bouguer, and so on. And the results of these corrections are presented in Tab.II-3.

Brief explanations of these corrections are explained in the following paragraphs :

(1) Tidal Correction

Gravimeters for geophysical prospecting in general are so sensitive that they also respond to the gravitational attraction of the sun and the moon and record periodic variations of the gravity values according to the relative location of these planets.

The vertical component of the tidal force caused by the sun and the moon are calculated by the following formula:

$$\Delta g = -3/2\,G\,M\,a / r^3 \{3(\sin^2\delta - 1/3)(\sin^2\delta - 1/3) + \sin 2\delta \sin 2\phi \cos\theta + \cos^2\delta \cos^2\phi \cos 2\theta\} \times 1.2 \ (gal)$$

where,

G : gravitational constant $= 6.67 \times 10^{-11}$ (m^3 / kg・sec^2)

M : mass of planets (moon : 7.348×10^{22}kg, sun : 1.9891×10^{30}kg)

a : distance from the center of the earth to the station

$= 6378388(0.99832 + 1.6835 \times 10^{-3}\cos 2\phi - 3.5 \times 10^{-6}\cos 4\phi)$ + altitude of the station(m)

r : distance from the center of the earth to the planet

(moon : 3.844×10^8 m, sun : 1.496×10^{11} m)

ϕ : latitude of the station

δ : declination of the planet

θ : hour angle of the planet.

(2) Drift Correction

In the case of spring-balance type gravimeter, the drift is caused by the creep of the spring material. The influence of the drift is minimized by assuming that the drift values vary in proportion to time. In this survey, the drift was less than 0.2 mgal/day.

(3) Terrain Correction

A topographic irregularity (hill, knoll, slope, valley, etc.) exert an gravitational attraction directly proportional to its density. It is necessary to compensate such effects, if the topographic features are close enough to cause distortions in the observed gravity. Accordingly, the distortions by topographic irregularity closer to the station have to be corrected in more detail.

The standard procedure of making corrections for such distortions is to estimate the average altitude within each divisions shown in Fig.II-5. Digital computers are used in common to calculate the correction values from the grid data of altitudes on topographic map, by dividing the area around the station into three groups, namely, far, middle, and near area.

i) Hammer's Method

The terrain corrections of far, middle, and near area were calculated by *Hammer's* method as shown the following form:

$$\Delta g = 2\pi G \rho / n \{ R_2 - R_1 + (R_1^2 + H^2)^{1/2} - (R_2^2 + H^2)^{1/2} \}$$

where,

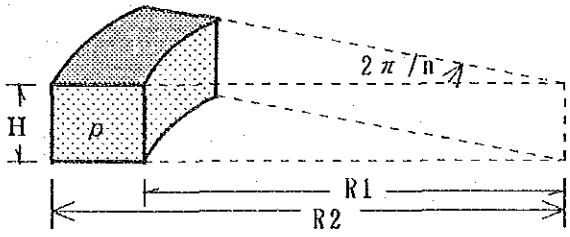

Δg : terrain correction value(mgal)
G : gravitational constant
ρ : correction density (g/cm^3)
R_1 : inner radius of the division(m)
R_2 : outer radius of the division(m)
H : altitude of station(m)
n : number of the divisions in a same circular ring.

The average altitude H of each division is estimated with surrounding four altitude data of the grid points, H_1, H_2, H_3, and H_4, illustrated as follows:

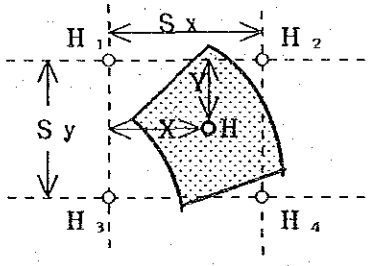

$$H = H_1 + (H_2 - H_1) X / S_x + (H_3 - H_1) Y / S_y + (H_1 + H_4 - H_2 - H_3) XY / S_x S_y$$

ii) Sketch Correction

The topographic features along the direction of maximum topographic undulation in a radius of 30 m at each station were sketched. By using the sketches, sketch correction was calculated with Hiroshima's method (1978, Hiroshima et al.). Expression and schematic figures are shown as follows:

$$\Delta g = 2G\rho \int_{D}^{R} \left\{ \tanh^{-1}\sqrt{(R^2 - X^2) / (R^2 + h^2)} - \tanh^{-1}\sqrt{(R^2 - X^2) / \{R^2 + (X\tan\beta + H - h - D\tan\beta)^2\}} \right\} dX$$

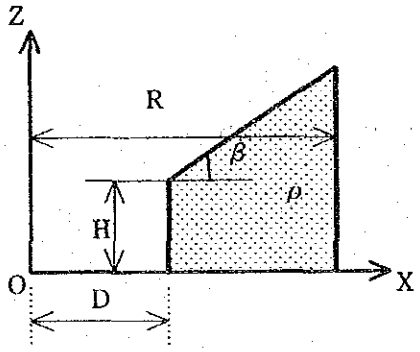

where, Δg : sketch correction value(mgal)

G : gravitational constant

ρ : correction density (g/cm³)

D : distance from station to cliff(m)

H : height of cliff(m)

β : angle of inclination of cliff (°)

R : referred range for calculation (30 m)

h : height of the weight of gravimeter(0.15m)

Since the range of terrain correction in this survey include water-covered area, the altitude of the water bottom was read and estimated the terrain correction by removing the gravity effect of water-mass.

(4) Elevation Correction

This correction consists of three parts: 1) the free-air correction, which accounts for the fact that each station has a different distance from the earth's center to the datum plane, 2) the Bouguer correction, which removes the effect of a presumed infinite slab of material between the horizontal plane of each station and the datum, and 3) the atmosphere correction, which removes the effect of the atmosphere.

Free-air correction: Free-air correction is estimated by the following expression:

$$\Delta g_1 = g_0 \{1 - R^2 / (R+H)^2\} = (2 g_0 HR + g_0 H^2) / (R+H)^2$$
$$\fallingdotseq 0.3086\ H \ \text{mgal}$$

where, g_0: gravity at mean sea level

H: altitude of station

R: average radius of the earth.

Bouguer correction: Bouguer correction can be expressed as:

$$\Delta g_2 = -2\pi G \rho H \fallingdotseq -0.0419\ \rho \cdot H \ \text{mgal}$$

where, G: gravitational constant

H: altitude of station (m)

ρ: density of slab (g/cm^3).

Atmosphere correction: Atmosphere correction can be obtained from the average atmospheric density model by use of the integral for the range 0 to 50 km. As shown in following figure, the relation between atmosphere correction and the altitude of the station can be assumed to be linear function ranging the altitude of less than 3 km. Therefore, we can express as the following form:

$$\Delta g_3 = 0.87 - 0.0965 \times 10^{-3} H \ (\text{mgal})$$

where, H: altitude of station.

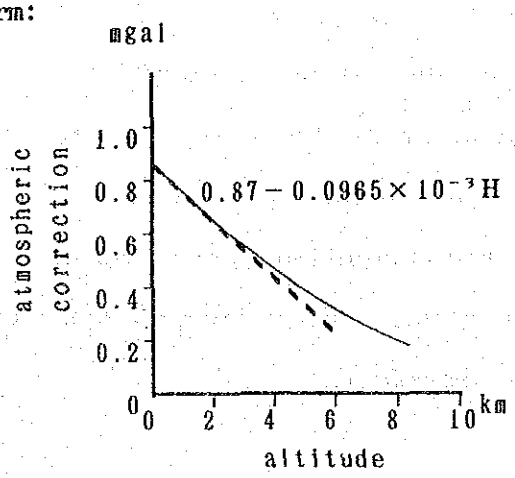

Because free-air, Bouguer, and atmosphere corrections are functions of the altitude of station, they are called elevation corrections and can be expressed as follows:

elevation correction: $\Delta g = \Delta g_1 + \Delta g_2 + \Delta g_3$

$$= (0.3086 - 0.0419 \cdot \rho - 0.0965 \times 10^{-3})\ H + 0.87 \quad (\text{mgal})$$

(5) Latitude Correction

Because of its rotation, the earth is not actually spherical. The shape can be approximated as an ablate spheroid with an eccentricity of 1/297. Both its departure from sphericity and its rotation cause the earth's gravitational acceleration to have a maximum value at the poles and a minimum at the equator. Therefore, the variation of the gravity value as a function of latitude of the station is reduced by using following International Formula on the International Ellipsoid.

$$\gamma = (a\,\gamma_E \cos^2\phi + b\,\gamma_P \sin^2\phi) \,/\, (a^2\cos^2\phi + b^2\sin^2\phi)^{1/2} \quad (\text{mgal})$$

where, a : equatorial radius of ellipsoid of revolution (6,378.14km)

b : polar radius of ellipsoid of revolution (6,356.18km)

γ_E : normal gravity at the equator of ellipsoid of revolution (978.032 gal)

γ_P : normal gravity at the polar of ellipsoid of revolution (983.218 gal)

This is the International Gravity Formula of 1967, which is adopted by IUGG (International Union of Geodesy and Geophysics) as the expression giving the normal gravity.

In practice, the expanded equation of the above is commonly used as the case of Phase II gravity survey :

$$\gamma = 978.031.85(1 + 0.005278895\sin^2\phi + 0.000023462\sin^4\phi) \quad (\text{mgal})$$

(6) Densities of Rock Samples

The terrain and Bouguer corrections for the reduction of gravity data require the knowledge of the densities of the rocks near the surface. Furthermore, the assumption of detailed underground density structure is necessary for the precise analysis of the data.

In this survey, 33 rock samples were collected at the surface (Fig.II-4) and wet densities were measured. The densities of rock samples were obtained from the following expression:

$$\rho = \frac{Wa}{Wa - Ww}$$

where, ρ: specific density

Wa: weight in air (after a day in water)

Ww: weight in water

Table II-2 shows the results of 33 sample measurements.

(7) Reduction Density

Bulk densities for twenty-five rock samples from ground surface range from 1.86 to 2.79 g/cm³. However, it is difficult to determine the formation density by only densities from the surface samples.

In this survey, the reduction density was determined by the following methods :

i) Gravity contour maps were drawn for three different densities, 2.2, 2.4, and 2.67 g/cm³. The correlation between gravity anomaly and topographic feature is shown in the following table. The gravity contour maps with densities of 2.4 and 2.67 g/cm³ were illustrated in Figures II-24 and II-25, respectively.

	correlation between gravity anomaly and topographic feature		
	$\rho = 2.2$	$\rho = 2.4$	$\rho = 2.67$
A [1)]	8	5	2
B [2)]	1	7	14

1) high gravity and high altitude, or low gravity and low altitude

2) high gravity and low altitude, or low gravity and high altitude

The density value, the gravity contours with which shows the least topographic effect is considered to be the best assumption value. For the survey, the best density value was about 2.4 g/cm³.

ii) The average density of twenty-five rock samples except ores was measured to be 2.55 g/cm³.

iii) Gravity is a function of the altitude of the station. When the altitudes and the corrected gravity values (after latitude and terrain corrections and reduction of gravity trends) are plotted on X-Y coordinates, the inclination of fitting line should represent the average rock density in the area. Fig.II-26 shows gravity versus altitude relation (G-H relation) for this survey, where the density was estimated as 2.405 g/cm^3 by least square fitting.

(8) Gravity Contour Maps

In order to make gravity contour maps, the gravity values transformed at 75 m square grid points were used. The weighted second-order orthogonal polynomial is adopted to estimate the gravity values at the grid points. The reference range for calculation of the gravity values at the grid points was ten times of the grid spacing. The gravity values were calculated only when there are more than six stations in fan-like area of 200 degrees with a center at the grid point.

1-2-5 Interpretation

The extraction of anomalies associated with individual subsurface sources from an observed gravitational field requires filtering operations. In this survey, the following techniques were used : surface fitting analysis, spectral analysis, and second vertical derivative analysis. Furthermore, techniques developed by Talwani was used to estimate two-dimensional and three-dimensional density structures.

(1) Surface Fitting Analysis

Gravity contour maps contain frequently not only gravity anomalies due to local geologic features in the survey area but also gravity trends by regional features.

In this area, the gravity trends decreased southward. The difference of strike direction of gravity contours between the northern half of the area and the southern (E-W dominant in the south and NE-SW dominant in the north) were observed. Therefore, third-order polynomial curve Z(X,Y) were adapted to remove the gravity trends.

Considering gravity data at grid points G(X,Y), we estimated three-order surface fitting curve Z(X,Y) by least squares method. Z(X,Y) and the residual values were presented by following form:

$$Z(X,Y) = -46.4285 - 0.88397836X + 1.16256697Y + 0.05999708X^2 + 0.11396378XY - 0.06440390Y^2 + 0.01809535X^3 + 0.06687063X^2Y + 0.09553135XY^2 + 0.05944291Y^3$$

$$(\text{Residual Value}) = G(X,Y) - Z(X,Y)$$

Here coordinates (X,Y) were expressed in a Cartesian coordinate system in topographic maps of Devision de la Cartographie and its X-axis lies along the east and Y-axis along the north.

The results are shown in Fig.II-27 and Fig.II-28.

(2) Spectral Analysis

Gravity contour maps in this survey involved anomalies with various wave lengths. By transforming such spatial gravity anomalies in frequency domain, it was possible to estimate the average depth of the sources of anomalies and to eliminate gravity anomalies attracted by the

source with spontaneous average depth (Spector and Grant, 1970).

Fig.II-30 shows the logarithmic energy spectrum of the gravity with frequency, f (cycle/km), where the spectrum can be approximated by using two regression lines. From the gradients of lines, the average depth (H) of buried source can be expressed by following formula:

$$H = -\frac{1}{4\pi} \cdot \frac{\Delta \log E}{\Delta f}$$

In this survey, the gravity field could be separated into regional component (average depth H_R=1,120 m) and near-surface component (average depth H_N=162 m).

From the results of the spectral analysis, the spectral maps for regional and near-surface component were drawn. In practice, the regional component, G_R, was expressed mathematically by using two average depth, H_R and H_N, and K_X, which was the differences of the crossing points between energy spectral axis and each regression lines as follows:

$$G_R(X, Y) = \frac{\int_{-\infty}^{\infty}\int_{-\infty}^{\infty} G(\xi, \eta) \cdot W(X-\xi, Y-\eta)\, d\xi\, d\eta}{\int_{-\infty}^{\infty}\int_{-\infty}^{\infty} W(\xi, \eta)\, d\xi\, d\eta}$$

where, weight function, W, can be expressed as follows:

$$W(X, Y) = \frac{1}{2\pi} \int_0^{\infty} \frac{f \cdot J_0(P \cdot f)}{1 + K_X \cdot e^{(H_R - H_N) \cdot f}}\, df$$

where, $P^2 = X^2 + Y^2$

Jo : Bessel function of first kind.

Shallow structure of spectral analysis, $G_N(X,Y)$ is obtained by subtracting the regional component, $G_R(X,Y)$, from the gravitational field, $G(X,Y)$ as following expression:

$$G_N(X, Y) = G(X, Y) - G_R(X, Y)$$

(3) Second Vertical Derivative Analysis

The second derivative of a gravity field can be shown to be the measurements of the curvature of the field. Plotting the second derivative will have the effect of distinguishing the gravitational anomaly from the local feature more conspicuously.

In practice, after the corrected gravity values are put on a map and contoured, the interpolated value of gravity is recorded at each grid point, the separation of which is denoted as S. Derivatives are computed at each point from rings centered around it. Averages are taken around rings having respective radii of S, $\sqrt{2}$S, 2S, and $\sqrt{5}$S as shown in following figure. In this study, the spacing of the grid was 150 m, which was a half of the depth of objective structure.

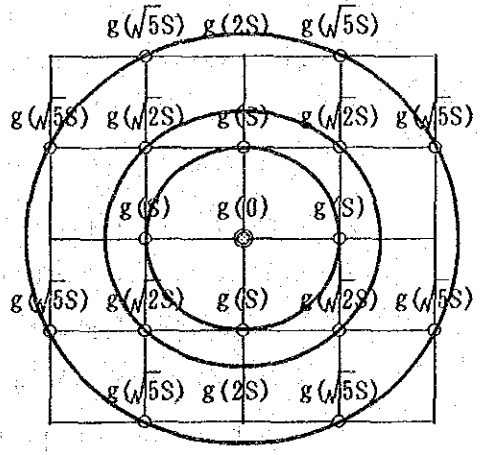

Grid Data for 2'nd Derivation

Derivatives are calculated with weight of distance as following expression.

$$g_x(0) = \frac{1}{24S^2}\{96g(0) - 72g(S) - 32g(\sqrt{2}S) + 8g(\sqrt{5}S)\}$$

(4) Three-Dimensional Simulation

Using residual gravity data at each grid point, two layered three-dimensional simulations were carried out. The density contrast between upper and lower layer is assumed to be 0.50 g/cm³. In practice, the least squares fitting method can be used to fit the gravity anomalies due to three-dimensional rectangular prisms to the observed data by varying the thickness of the prism. The dimension of the prism was 400 x 400 m.

Considering a rectangular prism with its center at the grid point, the vertical component of gravity at the grid point 0 is calculated as follows:

$$\Delta g = G\rho W^2 \{1/(R^2+d^2)^{1/2} - 1/\{R^2+(Z+d)^2\}^{1/2}\}$$

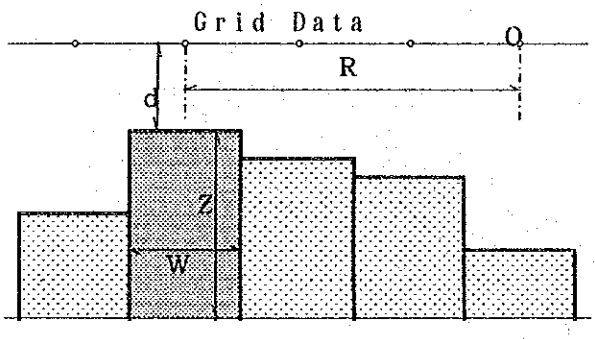

where,

G : gravitational constant

R : distance to the center of prism

ρ : density of prism($\Delta\rho = 0.50$)

Z : height from a base-surface to the top of prism

W : width of prism (150 m)

d : depth of the top of prism.

$$\Delta g_0 = 2\pi G\rho \left[Z - \left\{ (Z+d)^2 + W^2/\pi \right\}^{1/2} + (d^2 + W^2/\pi)^{1/2} \right]$$

The results of the calculation are given in Fig.II-35, where the contour lines indicate the depth of the top of second layer.

(5) Two-Dimensional Simulation

Two-dimensional simulations were carried out along two sections that were perpendicular to the structural trend of the area.

The periphery of any two-dimensional bodies is given by a polygon. The gravitational attraction caused by those bodies is compared with the measured gravity. Finally, the geometry of the disturbing body is adjusted from the starting model automatically by using optimization technique.

The gravitational attraction is calculated by Talwani's method. The vertical component of the gravity, Gv, at arbitrary point 0 on ground due to a polygon with a volume density ρ is given by :

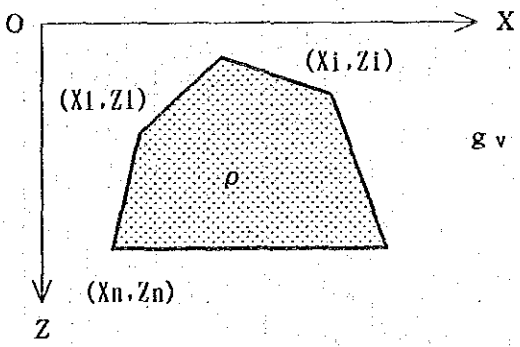

$$g_v = 2\rho G \sum_{i=1}^{n} \int_{Z_i}^{Z_{i+1}} \int_{\infty}^{X} \frac{Z}{X^2 + Z^2} \, dX \cdot dZ$$

where, ρ : density
G : gravitational constant.

In practice, multi-layered models based on geologic informations were used. The results are shown in Fig.II-33 and Fig.II-34.

CHAPTER 2 RESULTS OF THE SURVEY

2-1 IP Method

2-1-1 Results of Apparent Resistivity and IP Measurements

Average apparent resistivities and FE values measured for this project were shown in the following tables for each survey lines and each electrode separation n. Total average values in addition to the maximum and minimum values for each lines are also tabulated.

	Resistivity (Ω・m)								st. dev.
LINE	n=1	n=2	n=3	n=4	n=5	AVE	MAX	MIN	σ_n
HJ-1	39.6	40.6	48.6	57.4	67.6	49.9	155.0	19.0	26.9
2	56.7	60.6	68.4	85.2	95.3	72.0	177.0	26.6	37.2
TF-1	35.5	49.6	65.5	75.5	89.5	61.4	228.0	15.4	45.3
2	30.3	44.5	57.4	76.4	93.4	57.5	216.0	20.4	38.4
3	24.0	28.2	36.8	45.4	54.5	36.8	99.0	16.6	15.4
AK-1	59.7	92.0	131.2	158.4	202.2	126.5	963.0	26.0	125.3
2	38.5	46.0	63.7	68.6	80.3	57.5	145.0	21.5	34.8
LM-1	29.5	38.9	49.9	57.7	60.6	45.8	99.0	22.1	18.9
2	39.6	58.1	70.5	87.5	86.1	66.8	264.0	18.7	48.7
3	25.8	34.2	42.5	49.3	56.3	41.0	91.0	14.3	19.1
4	16.5	23.1	31.6	39.7	47.2	30.2	60.8	11.3	13.3
FZ-1	120.5	125.6	108.7	112.9	130.7	119.6	357.0	24.0	73.9
2	193.4	252.7	265.2	286.4	284.8	253.8	976.0	47.6	179.8
AVE	54.6	68.8	80.0	92.3	103.7	78.4			

Average apparent resistivity

	FE (%)								st. dev.
LINE	n=1	n=2	n=3	n=4	n=5	AVE	MAX	MIN	σ_n
HJ-1	2.0	2.0	2.4	2.9	3.4	2.5	6.6	0.6	1.4
2	1.4	1.4	1.4	1.7	1.7	1.5	2.6	0.8	0.3
TF-1	1.2	1.3	1.5	1.7	1.9	1.5	2.4	0.6	0.4
2	1.1	1.4	1.5	1.6	1.7	1.4	2.8	0.3	0.5
3	1.1	1.3	1.3	1.4	1.8	1.4	2.3	0.6	0.5
AK-1	1.3	1.4	1.5	1.5	1.7	1.5	3.3	0.0	0.8
2	1.4	1.5	1.6	1.6	1.8	1.5	2.5	0.6	0.5
LM-1	1.7	1.7	2.0	2.2	2.6	2.0	3.4	1.3	0.5
2	1.6	1.7	2.2	2.5	2.4	2.0	4.0	0.9	0.7
3	1.2	1.4	1.5	1.7	2.0	1.5	3.0	0.7	0.5
4	1.0	1.2	1.5	1.6	1.7	1.4	2.3	0.4	0.4
FZ-1	2.7	3.4	3.9	4.4	4.3	3.7	6.0	1.3	1.0
2	2.0	2.2	2.3	2.6	2.9	2.4	5.0	0.8	1.0
AVE	1.5	1.7	1.9	2.1	2.3	1.9			

Average FE value

Average (AVE), maximum (MAX) and minimum (MIN) values of each resistivity and IP lines are shown in addition to the standard deviation (σ_n). For example, the average resistivity value of Hajar HJ-1 is 39.6 ohm-m for n=1, and the average for n=1 to 5 is 49.9 ohm-m, with the maximum of 155 ohm-m and minimum of 19 ohm-m.

The apparent resistivity increases as n increases (like 54.6 ohm-m for n=1 and 103.7 ohm-m for n=5) for almost all the survey lines except LM-2, FZ-1 and FZ-2, and total average apparent resistivity is 78.4 ohm-m.

From the comparison of the average apparent resistivities among all

the survey lines, the minimum average apparent resistivity values was obtained at the line LM-4 (30.4 ohm-m), and maximum average apparent resistivity value was obtained at the FZ-2 of Frizem area (253.8 ohm-m). Also the average apparent resistivity values are as high as more than 100 ohm-m at the survey lines AK-1 of Akhlij-Oukhribane and FZ-2 of Frizem.

The standard deviation shows the variation of each values from the mean value, and the value increases when the variation of data is severe. For example, the standard deviation values of FZ-1, FZ-2 and AK-1 are greater than others, showing that the data of those three lines deviate more significantly than other lines. And the apparent resistivity values of LM=4 can be estimated from the table to be low with small deviation.

The average FE value also increases with the increase of n, and the average value of all the measurements is 1.9 %. More than 4 % FE values were obtained on the three survey lines HJ-1, LM-2, FZ-1 and FZ-2. As a whole standard deviation of FE is small, but the values more than unity were obtained on HJ-1, FZ-1 and FZ-2.

The results of the survey for each area are explained in the following paragraph :

(1) Hajar Block (Fig. II-6, II-7)

The station 10 of Hajar HJ-1 line was from 100 m west of the shaft of the Hajar mine, and the length of the line was 2 km north to south. the main purpose of the survey of this line was to check the validity of the resistivity and IP methods by carrying out the survey for known Hajar ore deposit.

Figure II-6 shows the pseudosection of the measured apparent resis-

tivity and IP values. Low resistivity values lower than 30 ohm-m were observed around the station 8, and also this part had as high as 4 to 5 % FE anomaly. Therefore, IP method showed its validity for the survey.

High apparent resistivity values of more than 50 ohm-m were observed at the northern part of the line (stations 12 to 18), and the values increased with the depth, but the FE values of this part was as small as 2 %.

HJ-2 situated 400 m east of HJ-1, and the length was 2 km north to south. Low apparent resistivity values of about 30 ohm-m were observed at the stations 4 to 6, but FE values were as small as 2 %, and the low resistivity and high IP anomaly zones like that of Hajar could not be found in this line. Apparent resistivity values of southern part increased in the same way as HJ-1.

(2) Tiferouine Block (Fig. II-8 to II-10)

The Tiferouine block was located 5 km east of Barrage Cavagnac, and made 3 resistivity and IP lines, namely TF-1, TF-2 and TF-3 from the west to the east.

The length of TF-1 was 2 km, running from the northeast to the south-east. The low apparent resistivity as low as 30 ohm-m were observed at the shallow part of the south of station 8, and high apparent resistivity of 50 to 200 ohm-m were obtained in the northern part of the line. As a whole, FE values were small except around station 8 and n=5 where around 2 % FE anomalies were observed.

The line TF-2 is parallel to the TF-1 and 1.5 km in length. The low apparent resistivity values were obtained in the southern part of the line, which was the same feature as the results of CSAMT method. IP anomaly could be seen at around station 10, but since the values were as

small as 2 to 2.8 and from the results of drilling nearby, this anomaly seemed to be corresponding to the disseminated zones. Those drillings were done according to the results of airborne magnetic survey, and found only disseminated zones around Tiferoune.

The line TF-3 was located about 800 m east and parallel to TF-2, and 2 km in length. Airborne magnetic anomalies have been discovered in northern part of this line, and low resistivity anomaly of CSAMT method was found around stations 12 to 15. Low apparent resistivity of about 40 ohm-m were obtained from the surface to up to n=4 to 5. The low apparent resistivity and strong IP values were obtained near the station 14, but the FE values were only 2.2 %.

(3) Akhlij-Oukhribane Block (Fig. II-11, II-12)

This block was located at the 2 km north west of Tiferouine, and 2 survey lines were provided. AK-1 was the longest 3.6 km survey line among all the lines, situating at the west of Akhlij and the direction was NE-SW. The low apparent resistivity values of less than 50 ohm-m were obtained around shallow part of stations 25 to 35. Although this low resistivity area was corresponding to the result of CSAMT survey, the FE values were as small as 0.5 %. Therefore, it will be hard to expect the same type of ore deposit as Hajar. Very high apparent resistivity values of more than 300 ohm-m were obtained around stations 16 to 21, and around 24. The FE values of this line were small except stations 8 to 18 and 22 to 25, where more than 2 % FE anomalies were obtained. The location of the former corresponds to the magnetic anomaly, but it will be difficult to see any relations to the ore deposit due to its high resistivity.

AK-2 was the 1.5 km line at east 900 m of AK-1. Low apparent resis-

tivity zones were observed near station 4 to 6, where low resistivities about 30 ohm-m were observed from n=1 to 5. Although the location of this anomaly coincides to the CSAMT anomaly and airborne magnetic anomaly, possibility of the existence of Hajar type ore deposit can not be expected due to its low FE values of 2 %.

(4) Lamrah Block (Fig.II-13 to II-16)

Four survey lines were prepared at the north to north west of Lalla Takerkoust, and were named LM-1 to LM-4 from east to west.

LM-1 was located just east of the main highway connecting Marrakech to Lalla Takerkoust, and the length was 1.5 km. Low apparent resistivity values of less than 30 ohm-m were obtained at the shallow part (n=1) of stations 5 to 13. In particular, the low resistivity part continues deeper near the station 6, where FE values were as large as 3.4 % and CSAMT low resistivity anomalies were also detected.

LM-2 was prepared along the west side of the highway, 2 km in length and N-S direction. The results were very similar to those of LM-1, and the apparent resistivity values at northern part of the line were smaller than those of LM-1 and continues from n=1 to n=5. And the FE anomaly was as small as 4 % at this low resistivity zone. On the contrary high apparent resistivity and low FE values were obtained at the southern part of the line, where more than 100 ohm-m resistivity values were observed at the stations 13 to 18.

LM-3 was located at the west side of N'Fis river flowing from the Barrage Cavagnac, and the length of the line was 3 km N-S. Low apparent resistivity anomalies were found at the shallow part (n=1 to 2) of the stations 2 to 15 and 21 to 25. Detected low apparent resistivity areas were well coincide with the results of CSAMT survey, and airborne mag-

netic anomalies. Especially, at the stations 5 and 6, the low resistivity zone is as deep as n=5. IP anomalies of deeper part (n=3 to 5) were obtained at the stations 7 to 12 and 18 to 24. Since the values were only 2 to 2.5 %, and corresponding resistivity values were not so small, these anomaly may not represent the Hajar type ore deposits. The low resistivity area of about 20 to 40 ohm-m around stations 22 and 23, seemed to be the extension of the low resistivity zone found in LM-1 and LM-2. This low resistivity zone was well coincide with the CSAMT low resistivity anomaly.

The line LM-4, 1.5 km in length, situated about 3 km west of LM-3. Low resistivity anomaly of CSAMT method and magnetic anomaly had been found around stations 6 to 12, and station 2 to 6 respectively. Apparent resistivity values near the surface were less than 20 ohm-m, and increased with depth. In particular, high apparent resistivity values of more than 50 ohm-m were observed at the stations 5 to 8 and 10 to 12 for n=4,5. The average apparent resistivity value of 30 ohm-m was the lowest among all the survey lines.

(5) Frizem Block

Two survey lines were laid out at the village Frizem, which was about 16 km WNW of Barrage Cavagnac. The line FZ-1, 2 km in length, was running ENE-WSW at the north of Frizem, and FZ-2 was 2 km in length and parallel to the FZ-1 and 900 m south.

Apparent resistivity values of FZ-1 fluctuated severely, and the average was as high as 120 ohm-m. Around station 7, a dyke shaped structure with low resistivity of 20 to 30 ohm-m and strong FE anomaly of 5 to 6 % were discovered. Higher apparent resistivity values were observed form the east of station 8, but slightly lower resistivity values of 50

ohm-m and high FE of 5 % were found around station 11 to 12, n=4,5.

The highest average apparent resistivity value of 250 ohm-m was obtained from FZ-2. High apparent resistivity values of more than 200 ohm-m were obtained at the west of station 10, and stations 14 to 15, n=2,5. Apparent resistivity values of less than 100 ohm-m, which were relatively small for this line, were obtained at the shallow part of stations 12 to 14, and stations 16 to 17. Strong FE anomaly of more than 4 % were obtained at stations 2 to 5, n=3,5.

(6) Apparent Resistivity Map

Measured apparent resistivity maps are shown in PL.II-3 to PL.II-7, and measured FE maps are shown in PL.II-8 to PL.II-12. These plain maps were made for reference purpose, because in some area the separation of each survey lines apart too much to draw contour lines.

From the PL.II-3 which shows apparent resistivity map for n=1, a high resistivity zone can be seen from station 20 of AK-1 to station 5 of TF-1, in addition to stations 5 to 12 of AK-1 and southern part of Hajar. There were quite few low resistivity zones on the shallow part corresponding to n=1, but less than 20 ohm-m were obtained at the northern part of TF-1 to TF-3, and north of LM-3.

Similar features are found for n=2 (PL.II-4), but the area of high resistivity zones increased at the southern part of LM-2 and LM-3. For n=3 (PL.II-5), high resistivity zone increased more especially around the middle of AK-1 line.

Southern areas of Hajar and Lamrah blocks were resistive, and northern areas were conductive for n=4 (PL.II-6). In particular, southern part of LM-2 showed very resistive zone.

The map for n=5 was similar to that of n=4, but the increase of

resistive zones was clear. Low resistivity values of less than 30 ohm-m were obtained only at HJ-2 and LM-2.

The fluctuation of the apparent resistivity values of Frizem block was more severe than that of western area, and very hard to represent data as a plan map. The low resistivity zone of the western side of FZ-1 seems to continue to FZ-2. But the high resistivity zone at the western part of FZ-2 cannot be continued to FZ-1.

(7) IP Map

Maps of FE values were shown in PL.II-8 to PL.II-12, corresponding to the separation constant n of 1 to 5 respectively. In general, FE values increased with n. There were 3 percent FE for n=1 at HJ-1 line, and this high IP anomaly zone was more clear as the increase of n. FE anomaly of more than 3 percent could be found at LM-2 for n=4, and at LM-1 and northern end of AK-1 for n=5.

Small FE values obtained at the east of FZ-2 seemed to continue to around station 12 of FZ-1. High FE anomalies could be seen at the west side of FZ-1 and FZ-2, and so the zones seemed to be continuous from south to north. But the continuity of high FE zone of more than 5 % could not be fully understood by using only two survey lines. This high FE zone seemed to correspond to conductive area at FZ-1 but corresponds to resistive area of more than 200 ohm-m at FZ-2.

2-1-2 Two Dimensional Simulation Results

Low apparent resistivity and strong IP anomalies were found at HJ-1, LM-1, LM-2 and FZ-1. The results of two dimensional computer interpretations were shown in Fig.II-2 to II-23 (PL.II-13 to II-17).

(1) Hajar Block

Very low resistivity and string IP effect were observed at around station 8 of HJ-1. To investigate the structures of this anomaly, two dimensional computer simulations were carried out. Starting from the initial model constructed from the apparent resistivity pseudosection and other informations, analytical model was obtained by trial and error way of changing the model to fit to the field data. And after about 20 times of iteration, final analytical model was obtained as shown in Fig.II-19 (PL.II-13). Low resistivity and high IP anomaly of HJ-1 was well represented by the model. For example, 30 ohm-m contour of the figure well represents the feature of the 30 ohm-m contour of the field data (Fig.II-6). As the final result, the conductive structure of 12 ohm-m with FE of 20 % was obtained at depth 200 m of station, and the northern part of the structure was deeper than the southern part. And the depth of the 200 ohm-m resistive basement becomes shallower at the southern part, and deeper at the station 8 where the conductive structure was analyzed. That is the reason of the high apparent resistivity of the southern part of HJ-1. A structure with low resistive (15 ohm-m) and relatively small FE anomaly (3%) was analyzed around the stations 8 to 12, in the 50 to 100 m depth.

(2) Lamrah Block

Since low resistivity and high IP anomaly values were detected at Lamrah LM-1 and LM-2, in addition to the CSAMT low anomaly near by, computer simulation was performed to check the shape, resistivity and FE of the anomaly. The results of the simulation for LM-1 and LM-2 are shown in Fig.II-20 and Fig.II-21 respectively. Low resistivity structure around stations 5 to 6 in Fig.II-13 was well expressed in Fig.II-20. The

result of the simulation showed that the conductive surface of 20 ohm-m resistivity becomes deeper at station 6, and beneath of the layer was the conductive structure of 10 ohm-m. The FE of the conductive structure was 20 % at the depth of 200 m. The low resistive (10 ohm-m) and high FE (15%) structure was analyzed at the depth 200 m, and the size of which seemed larger than LM-1.

(3) Frizem Block

The low resistivity and high FE (5 to 6 %) structure was found at the Frizem FZ-1. Although the shape of the contours of resistivity pseudosection was so complicated that it was very difficult to make the initial model, the final analytical structure was obtained after several tens of iterations. The simulated apparent resistivity contours well represented the field data, but the FE contour represented only high FE part of the figure. A structure of low resistivity (20 ohm-m) and moderate FE (3 %) was analyzed at station 7, depth 50 to 200 m, and beneath of it was a structure of 20 ohm-m and 25 % FE. In particular, there was an analyzed structure of moderate resistivity of 50 ohm-m but high FE of 20 % adjoining the conducting structure.

Highest average apparent resistivity was obtained from FZ-2, and therefore, the resistivity of analyzed basement was as high as 500 ohm-m. The structure of moderate resistivity of 50 ohm-m and high FE of 20 % were analyzed at the west end of the line, and this structure seems to be corresponding to the structure of station 2 of FZ-1.

2-2 Gravity Method

The results of the interpretation are shown in the following maps.

Fig.II-24 Gravity Contour Map (ρ =2.4 g/cm^3)

Fig.II-27 Third-order Surface Fit Map

Fig.II-28 Third-order Residual Map

Fig.II-29 Second Vertical Derivatives Map (S=150 m)

Fig.II-30 Energy Spectrum

Fig.II-31 Results of Spectral Analysis (Shallow structure)

Fig.II-32 Results of Spectral Analysis (Deep structure)

Fig.II-33 Cross Section of A-A'

Fig.II-34 Cross Section of B-B'

Fig.II-35 Structure Contour Map on the Top of the Basement

2-2-1 Gravity Contour Map (ρ=2.40, Fig.II-24)

Fig.II-24 shows the Bouguer anomaly map obtained with reduction density 2.4 g/cm^3.

In this survey area, Bouguer anomaly values ranged from -37 mgal to -55 mgal, which decrease southeastward. Linear contours along E-W direction in the southeastern part of the survey area and NE-SW in the northwestern part.

The features of contours developing to the north showed the low Bouguer anomaly, and those developing to the south showed high anomaly, because of the high Bouguer anomaly in the north and low in the south.

The characteristics of the gravity contour map were as follows:

i) Contours developed E-W direction around Tiferouine district. The gravity attraction increased northward to Oukhribane district with the

gradient of 4 mgal/km.

ii) A high Bouguer anomaly zone spread along NW-SE direction around the south of Oukhribane district. Low anomaly zone that was roughly parallel to the southern side of the high anomaly was recognized.

iii) Contours striking along WNW-ESE direction in the east of Akhlij district indicated a high anomaly, where the gradient was 3 mgal/km.

iv) Roughly linear contours with the gradient of 2 mgal/km striking from Amzourh to Lamrah district were observed. Gradient in the western side of these contours was gentle.

2-2-2 Third-Order Residual Map (Fig.II-28)

Gravity contour map (Fig.II-24) was effected by large-scale and deep structural trends. It is efficiently to remove these trends for the purpose of mineral exploration with the depth of less than a few hundred meters.

Therefore, the third-order residual values (Fig.II-28) from which the gravity trends was removed were used to obtain the sub-surface density structure for this survey. As shown in Fig.II-28, irregular and complex contours were observed. Gravity variations by shallower density structure were usually exaggerated that it was easy to compare with the geological structure.

High and low Bouguer anomalies in the third-order residual map were as follows:

i) Akhlij High Anomaly

This high anomaly zone was located from the north of Akhlij to the southeast. Despite the zone seemed to be spreading northward in the east of Akhlij, the feature of the zone was not clear at the edge of the survey area. The values of residual Bouguer anomaly were more than 1.5 mgal, which was maximum in this survey area.

ii) Oukhribane High Anomaly

This belt-like high anomaly zone was located in the south of Oukhribane, which spread along NW-SE direction. At the center of the zone, the feature of the gravity anomaly was massive. In the southern part of the anomaly, the direction of strike-axis was westward. The southern part of this area corresponded to the high apparent resistivity zone obtained by the IP method. The maximum residual value exceeded 1 mgal in the northern part of the high anomaly zone.

iii) Amzourh High Anomaly

The high anomaly formed a crude horseshoe shape in the north of Amzourh. The maximum residuals are as much as 0.8 mgal in the eastern part of the zone.

iv) Hajar High Anomaly

A high anomaly zone from the south of the Hajar mine to the southeastern edge of the survey area were observed, where the maximum residuals exceeded 1 mgal.

v) West Oukhribane Low Anomaly

This trough-like anomaly zone extended from the northwest of Oukhri-

bane to the south. Furthermore, the zone diverged from the west of Oukhribane to the south-southeast, which was roughly parallel to the Oukhribane high anomaly zone. Massive low anomalies sparsely distributed with the residuals of less than -0.7 mgal.

vi) West Hajar Low Anomaly

From the west of Hajar mine, the trough-like anomaly zone extended southward, and reached to the east of Tiferouine. The center of the low anomaly zone with the residuals of less than -0.7 mgal was located at the west of Tiferouine.

vii) East Lamrah Low Anomaly

Massive low anomaly zone was found at the east of Lamrah. The low anomaly reached to the northern edge of the west Oukhribane low anomaly. The residuals were less than -1 mgal, which were the minimum in this survey.

2-2-3 Energy Spectrum (Fig.II-30)

The result of power spectrum analysis of the gravity contour map (Fig.II-24) was expressed in logarithmic energy spectrum as shown in Fig.II-30. According to the two regression lines of energy spectrum, the spectrum could be divided to regional components (average depth: 1,120 m) and near-surface components (average depth: 162 m).

In practice, the depth means the average depth of basement that cause gravitational attraction. Therefore, the range of the actual depth may be wide. On the other hand, the depth is also affected by the configuration of density distribution. In the case of the presence of a widespread thin layer in near surface, the gravity attraction shows

a long-period in the energy spectrum, which is extracted to be deeper structure.

The depths of the dominant structure for gravity attraction in this survey area were divided as following table.

component	average depth	range of depth	relationship with geologic feature
regional component	1,120 m	600m or more	• regional geologic structure
near-surface component	162 m	near surface ~ 600m	• undulation of basement • average thickness of sediments • density variations of rocks

2-2-4 Results of Spectral Analysis for Shallow Structure (Fig.II-31)

Fig.II-31 shows the residuals excluding long-period gravity component from gravity contour map (Fig.II-24) and exaggerating the gravity distribution by shallower structure with the average depth of 162 m (surface to about 600 m). Short-period gravity anomalies, showing gentle undulations of contours in Fig.II-24 were cleared.

The gravity distribution in this map indicated a dominant direction of N-S in the western part of the survey area and E-W in the eastern part.

2-2-5 Results of Spectral Analysis for Deep Structure (Fig.II-32)

Fig.II-32 shows the gravity anomalies excluding short-period gravity component of gravity contour map (Fig.II-24) and exaggerating the gra-

vity distribution by deeper structure with the average depth of 1,120 m (more than 600 m).

The feature of the long period component of the gravity distribution can be considered to be the large-scale gravity trends around this area and undulation of the depth of basement.

2-2-6 Second Vertical Derivatives Map (Fig.II-29)

The second vertical derivatives of a gravity field showed the feature of the curvature of the field and the shallow density structure. By considering the grid spacing of 150 m, the map seemed to be reflecting the density structure with the depth of few hundred meters. The boundary of the density structure was emphasized by the steep contours in this map.

Inasmuch as the objective depth was similar, the feature of the second vertical derivative map was similar to the results of spectral analysis for shallow structure. Despite there could be seen a lot of short period anomalies caused by the density structure near the surface in the spectral analysis map, such anomalies were smoothed in the second vertical derivatives map.

Gravity anomalies in this map was dominated along NW-SE direction around Oukhribane and N-S in the east of Akhlig.

2-2-7 Structure Contour Map on the Top of the Basement (Fig.II-35)

The most suitable three-dimensional density structure with a density contrast of 0.5 g/cm^3 was shown in Fig.II-35. The contours showed the depth to the gravity basement.

From the outcrops in Oukhribane, Akhlij and Amzourh, the Hajar horizon was considered to be the gravity basement. The density contrast was

decided by referring the rock samples.

The distribution of gravity basement was very similar to the distribution of high and low anomalies shown in three-order residual map (Fig.II-28).

Main configurations of the gravity basement were compiled in following table.

Gravity anomalies in 3'rd-order residual map	Uplift area of basement	depressed area of basement
	10 m or less	60 m or more
A k h l i j H. A.	North Akhlij~East Akhlig	———
Oukhribane H. A.	Northwest Oukhribane~ North Tiferouine	———
A m z o u r h H. A.	Northwest Lamrah	———
H a j a r H. A.	South Hajar	———
W e s t L. A. Oukhribane	———	Southwest ~West Oukhribane
West Hajar L. A.	———	Southwest Hajar Northeast Tiferouine
East Lamrah L. A.	———	East Lamrah
t h e o t h e r	South Taguennza	———

H. A. : high gravity anomaly, L. A. : low gravity anomaly.

2-2-8 Cross Sections of A-A' and B-B' (Fig.II-33 and Fig.II-34)

As the main strike of the geological structure were along NW-SE direction in the central part of the survey area, cross sections were prepared along NE-SW.

Cross sections of the third-order residuals, density structure, and geological structure were illustrated in Fig.II-33 and Fig.II-34.

As for the density model, the three layered model with the first layer of ρ=2.2 of the Quaternary sediments, the second layer of ρ=2.70 of the Hajar horizon and the lower Imarine horizon, and the third layer of ρ=2.76 of the lower Hajar horizon was considered reasonable as compared with densities obtained by rock samples. They were named low, middle, and high density formations, respectively.

i) Cross Section of A-A' (Fig.II-33)

Cross section of A-A' was from Amzourh northeastward to the southeast of Taguennza. Low resistivity and IP anomaly zone detected by IP method was located around Lamrah, the central to the northern part of the cross section.

The third-order residuals along this section were passing through the Amzourh high anomaly, gentle low anomaly zone around Lamrah, and small-scale high anomaly in the northern edge of the profile. The gravity values were comparatively long-period and small amplitude.

Corresponding to the positive anomaly, an uplift of high density formation to the 200 m depth and an uplift with 400 to 500 m around Lamrah were estimated. The middle density formation uplifts to near the ground surface around Amzourh. The low density thin formations were distributed around Lamrah. The thickness increased northward in the north edge of the profile. Low resistivity and IP anomaly zones around Lamrah coincided with the zone of less gravity variation.

ii) Cross Section of B-B' (Fig.II-34)

The cross section B-B' extended from the southwest of Oukhribane to the northeast of Akhlij, which was parallel to the cross section A-A'.

The cross section of third-order residuals along this profile was

passing through the west Oukhribane low anomaly at the west of the profile, Oukhribane high anomaly at the central, gentle low anomaly, and to Akhlij high anomaly. The gravity values of this section were changing in both amplitude and gravity wave length.

The depth of the high and the middle density formations was smaller at the center of the profile. The high density formation was continued below the low density formation in the south and was tilted to the north at steep angle to the depth of more than 500 m in the central. Despite the existence of the uplift in the north, the top of the high density formation was analyzed to be the depth of 300 to 400 m. The middle density formation was distributed in the central and the north. The thickness of low density formation was large in the south and small around Akhlij.

The gravity basement uplifted at the central part of the profile corresponded to the Hajar horizon. Area without low density formation coincide with the outcrops zone of the lower Imarine horizon (Pelitic semischist with limestone).

COOPERATIVE MINERAL EXPLORATION
IN
HAOUZ CENTRAL AREA, MOROCCO
(PHASE II)

Fig. II-1 Geophysical Survey Area

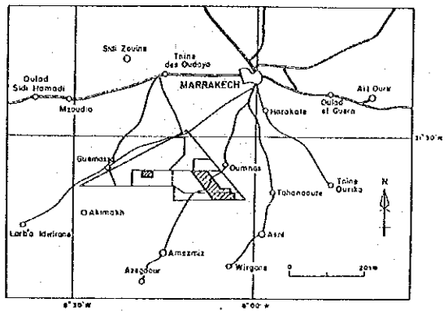

JAPAN INTERNATIONAL COOPERATION AGENCY
METAL MINING AGENCY OF JAPAN
FEBRUARY 1989
Prepared by MINDECO

0 5,000m
Scale 1:100,000

LEGEND

IP Survey Line

Gravity Survey Area

COOPERATIVE MINERAL EXPLORATION
IN
HAOUZ CENTRAL AREA MOROCCO
(PHASE II)

FIG. II-2
IP SURVEY AREA WITH SURVEY LINES

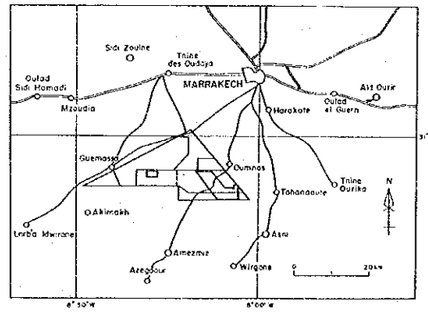

JAPAN INTERNATIONAL COOPERATION AGENCY
METAL MINING AGENCY OF JAPAN
FEBRUARY 1989
Prepared by MINDECO

0 2,500m

Scale 1 : 25,000

LEGEND

0 5 Station Number
Survey Line

HJ	Hajar
TF	Tiferouine
AK	Akhlij – Oukhribane
LM	Lamrah
FZ	Frizem

COOPERATIVE MINERAL EXPLORATION
IN
HAOUZ CENTRAL AREA, MOROCCO
(PHASE II)

Fig II－3
LOCATION MAP OF GRAVITY SURVEY

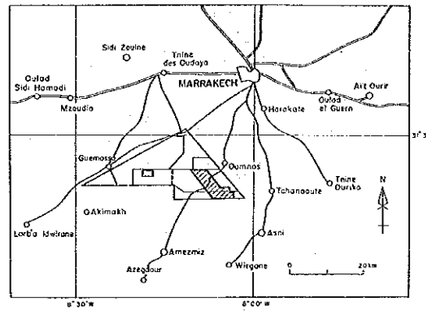

JAPAN INTERNATIONAL COOPERATION AGENCY
METAL MINING AGENCY OF JAPAN
FEBRUARY 1989
Prepared by MINDECO

0 2,500m

Scale 1 : 50,000

LEGEND

● HS－1 Boring Site

315 Station Number
○ Gravity Station

COOPERATIVE MINERAL EXPLORATION
IN
HAOUZ CENTRAL AREA, MOROCCO
(PHASE II)

Fig. II -4 Locations of Rock Samples

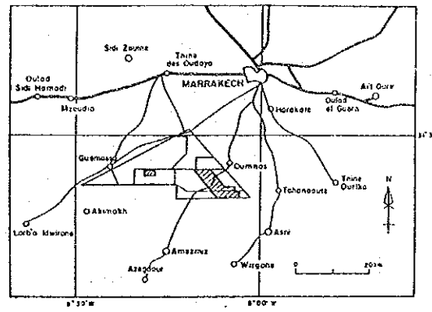

JAPAN INTERNATIONAL COOPERATION AGENCY
METAL MINING AGENCY OF JAPAN
FEBRUARY 1989
Prepared by MINDECO

0 5,000m
Scale 100,000

LEGEND

- 26 Location of Sampling
- IP Survey Line
- Gravity Survey Area

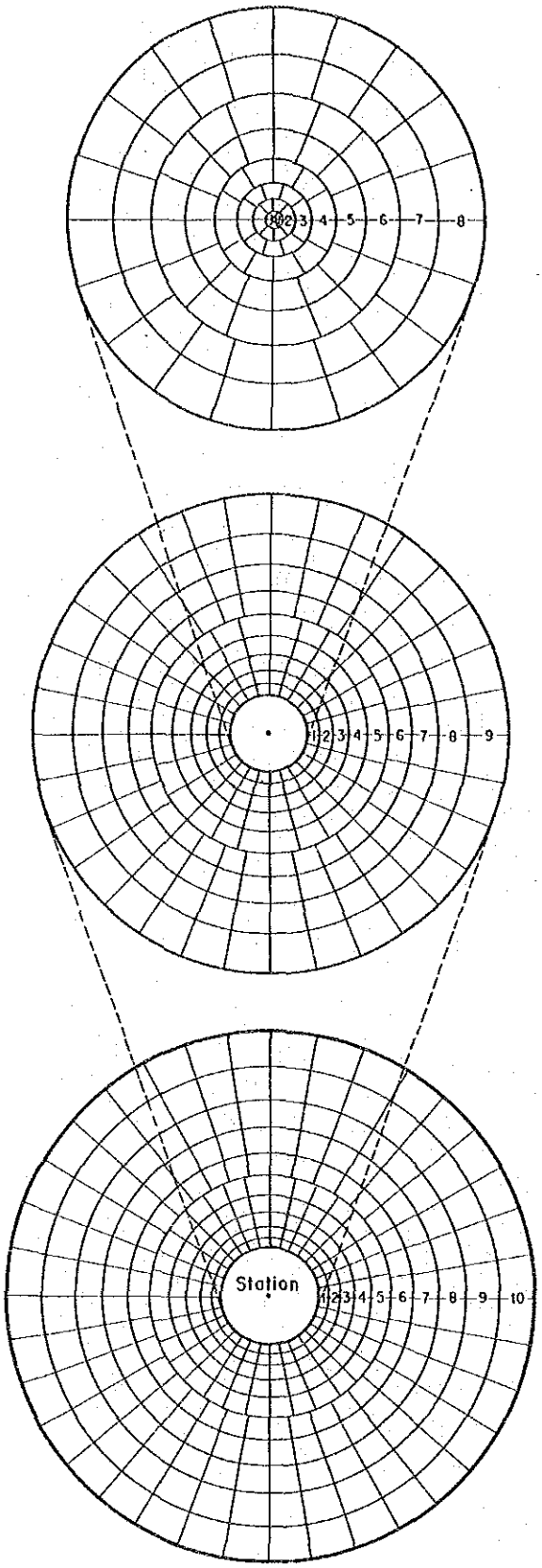

【NEAR】 Using 150m grid data

No.	R1 ～ R2	n
	m ～ m	
1	30 ～ 100	6
2	100 ～ 200	8
3	200 ～ 350	10
4	350 ～ 550	12
5	550 ～ 800	16
6	800 ～ 1,150	16
7	1,150 ～ 1,550	20
8	1,550 ～ 2,000	20

【MIDDLE】 750m grid data

No.	R1 ～ R2	n
	m ～ m	
1	2,000 ～ 2,500	24
2	2,500 ～ 3,000	24
3	3,000 ～ 3,600	24
4	3,600 ～ 4,300	24
5	4,300 ～ 5,100	24
6	5,100 ～ 6,000	32
7	6,000 ～ 7,100	32
8	7,100 ～ 8,400	32
9	8,400 ～ 10,000	32

【FAR】 3,000m grid data

No.	R1 ～ R2	n
	m ～ m	
1	10,000 ～ 12,000	32
2	12,000 ～ 14,000	32
3	14,000 ～ 17,000	32
4	17,000 ～ 20,000	32
5	20,000 ～ 24,000	32
6	24,000 ～ 28,000	36
7	28,000 ～ 33,000	36
8	33,000 ～ 38,000	36
9	38,000 ～ 44,000	36
10	44,000 ～ 50,000	36

Fig. II-5 Annular Segments for Terrain Correction

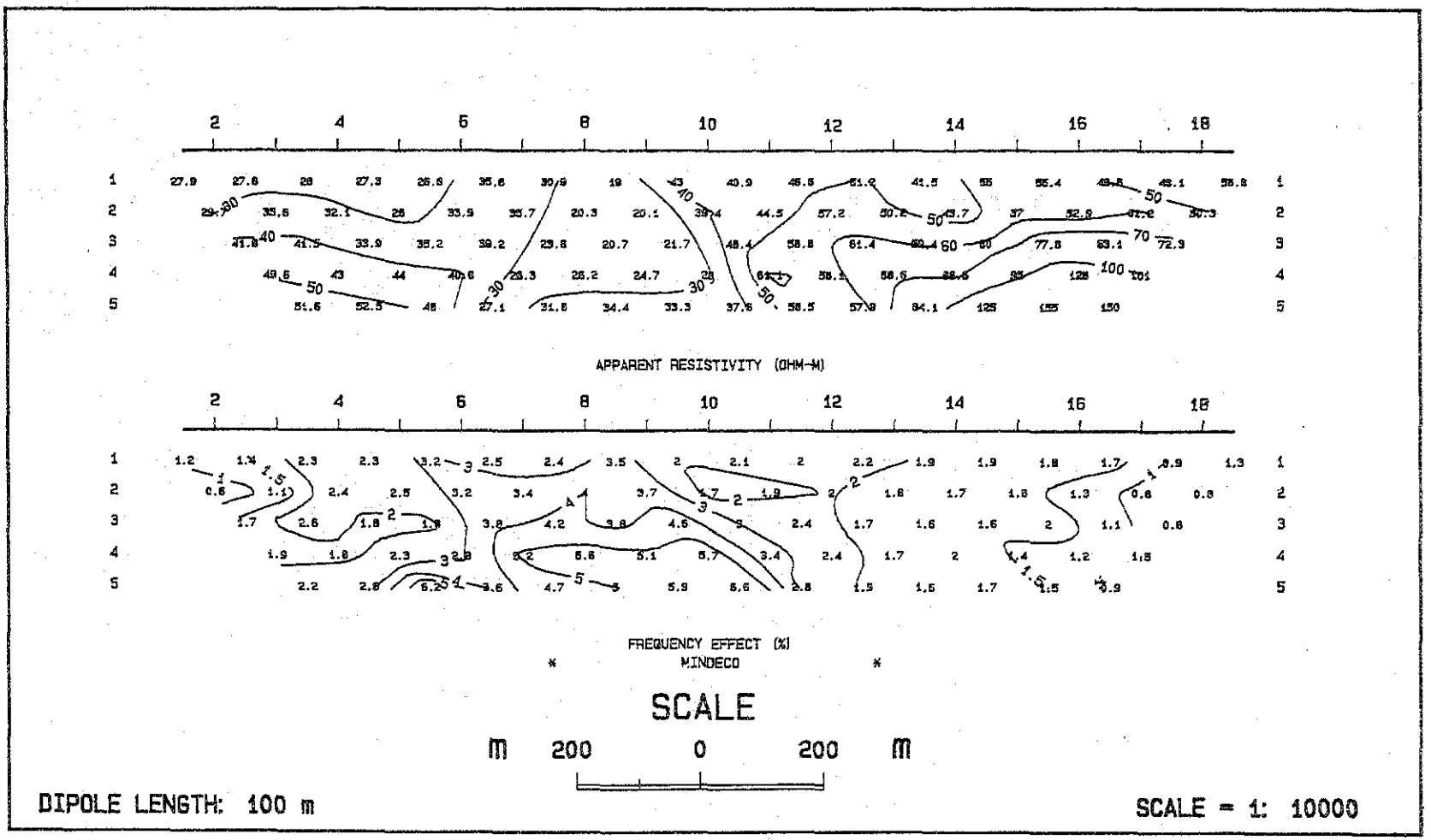

Fig. Ⅱ-6 Apparent Resistivity and PFE Pseudo Section (Line HJ-1)

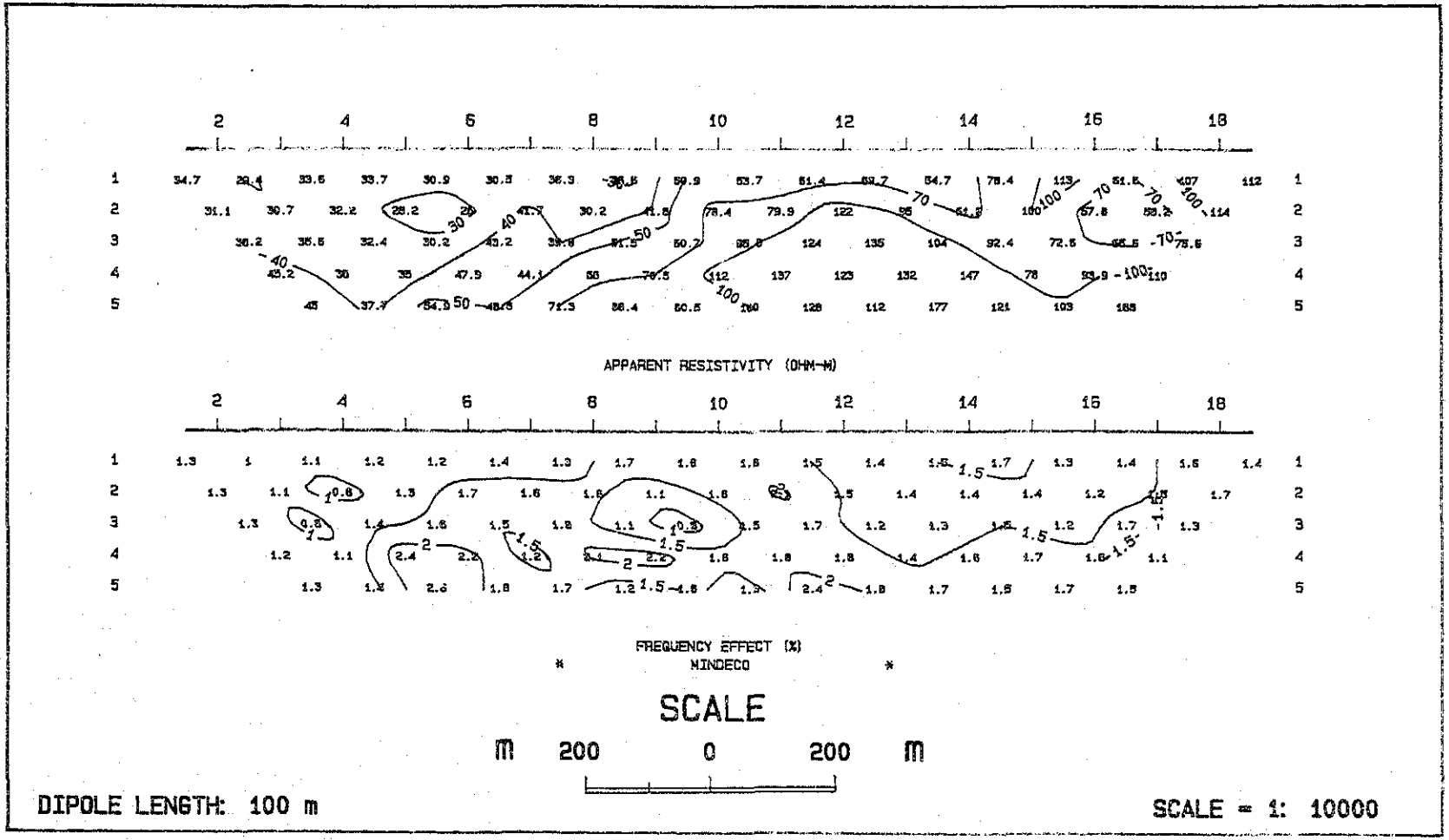

Fig. Ⅱ-7 Apparent Resistivity and PFE Pseudo Section (Line HJ-2)

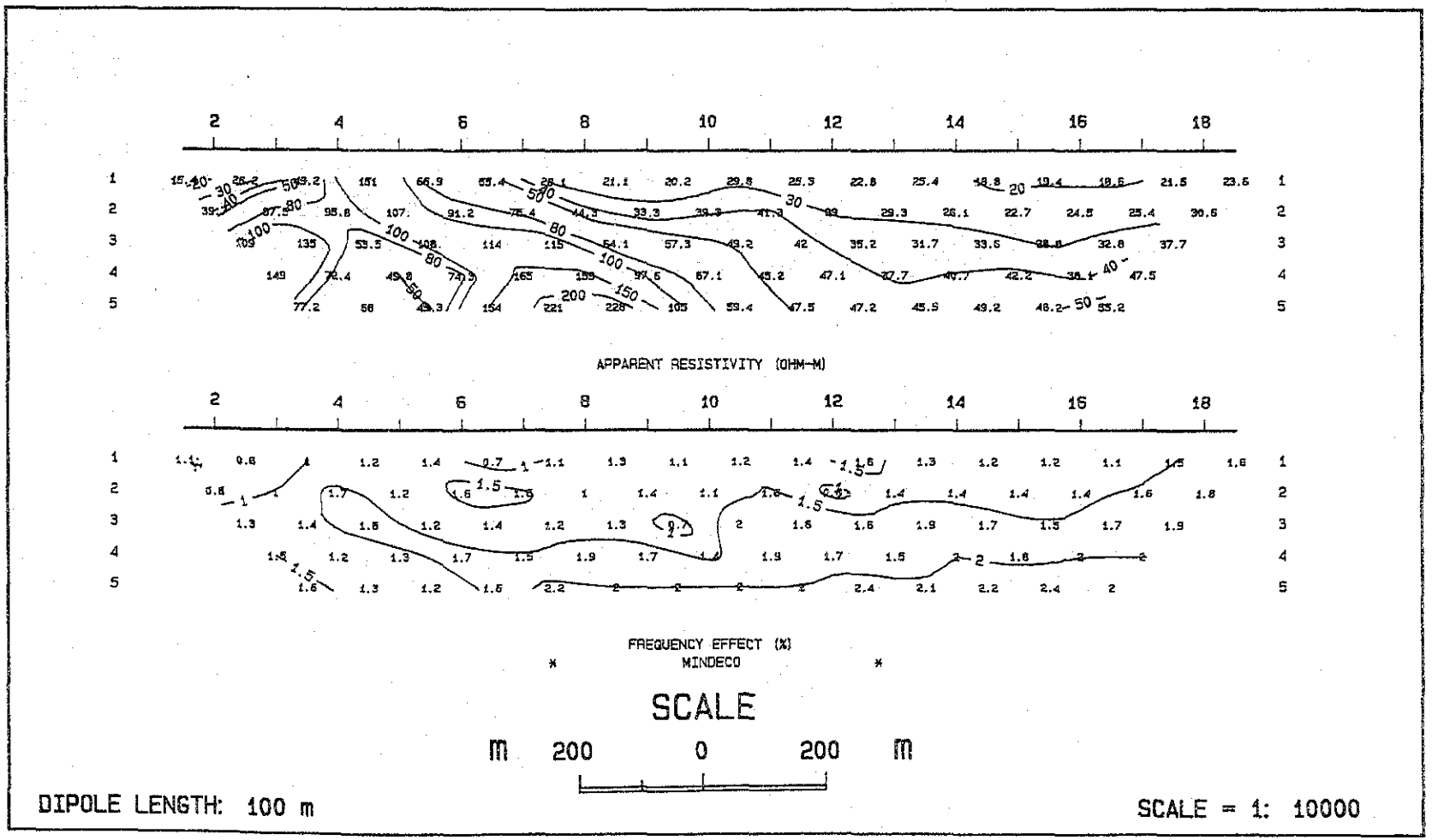

Fig. Ⅱ-8 Apparent Resistivity and PFE Pseudo Section (Line TF-1)

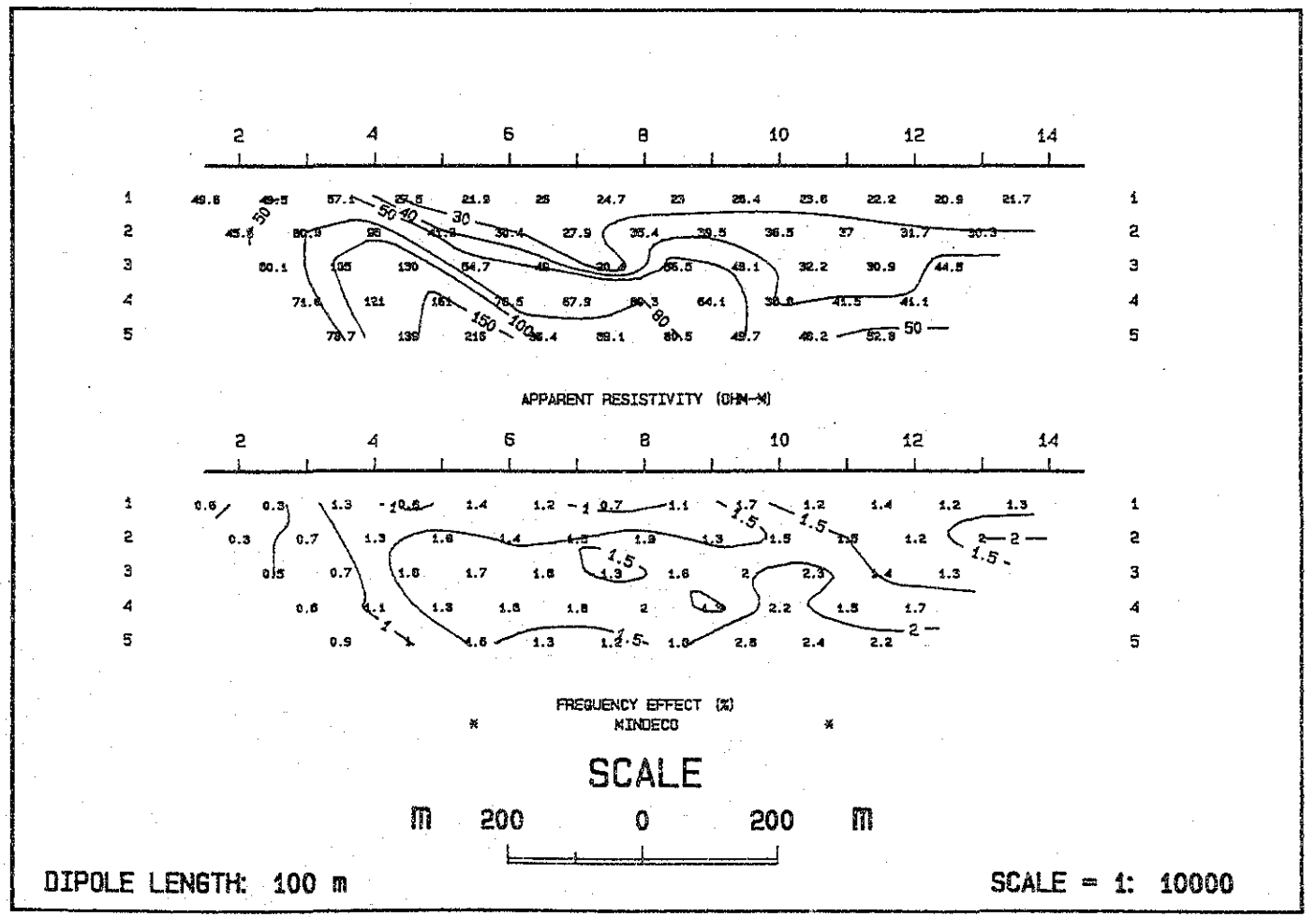

Fig. Ⅱ-9 Apparent Resistivity and PFE Pseudo Section (Line TF-2)

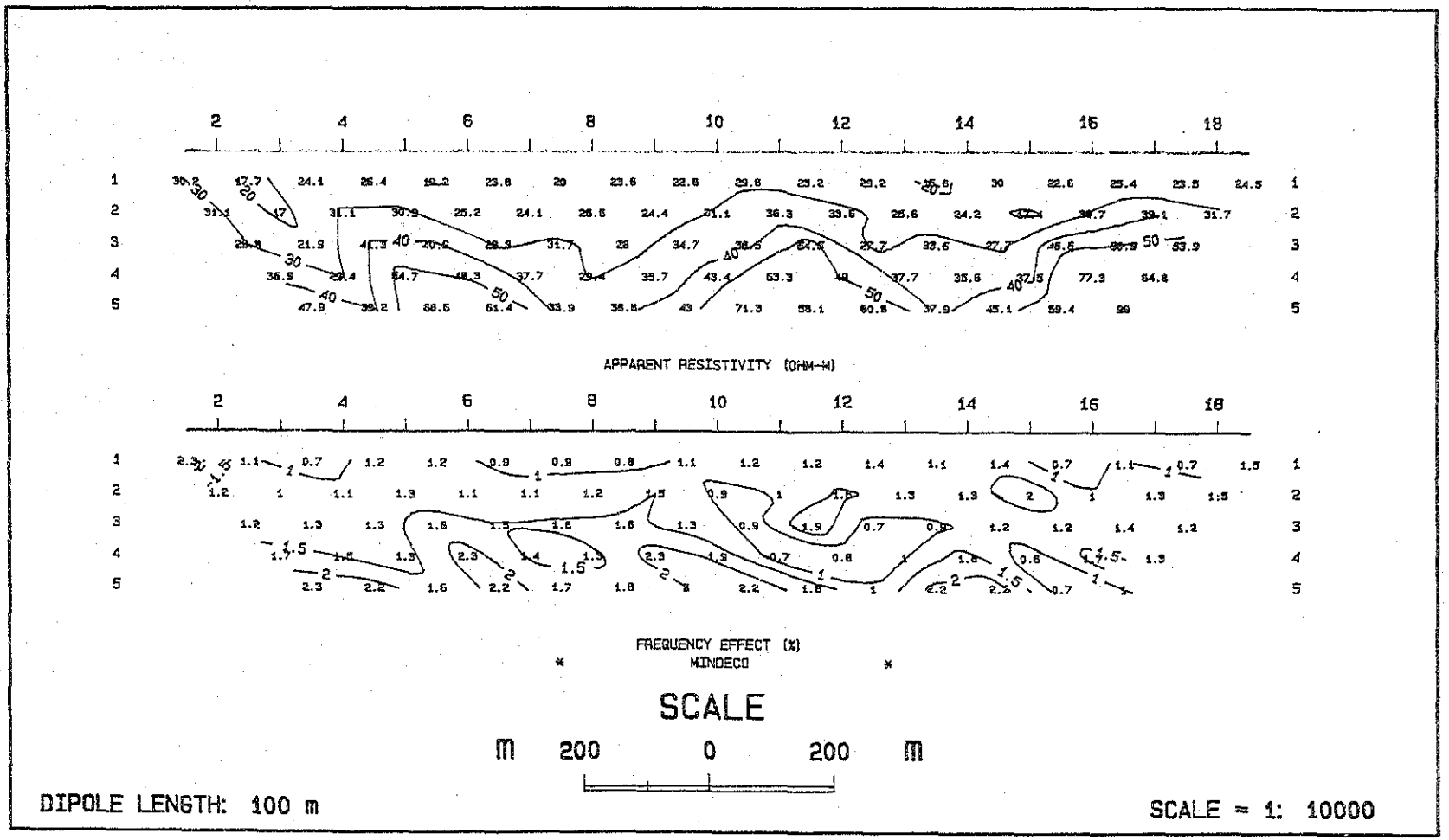

Fig. II-10 Apparent Resistivity and PFE Pseudo Section (Line TF-3)

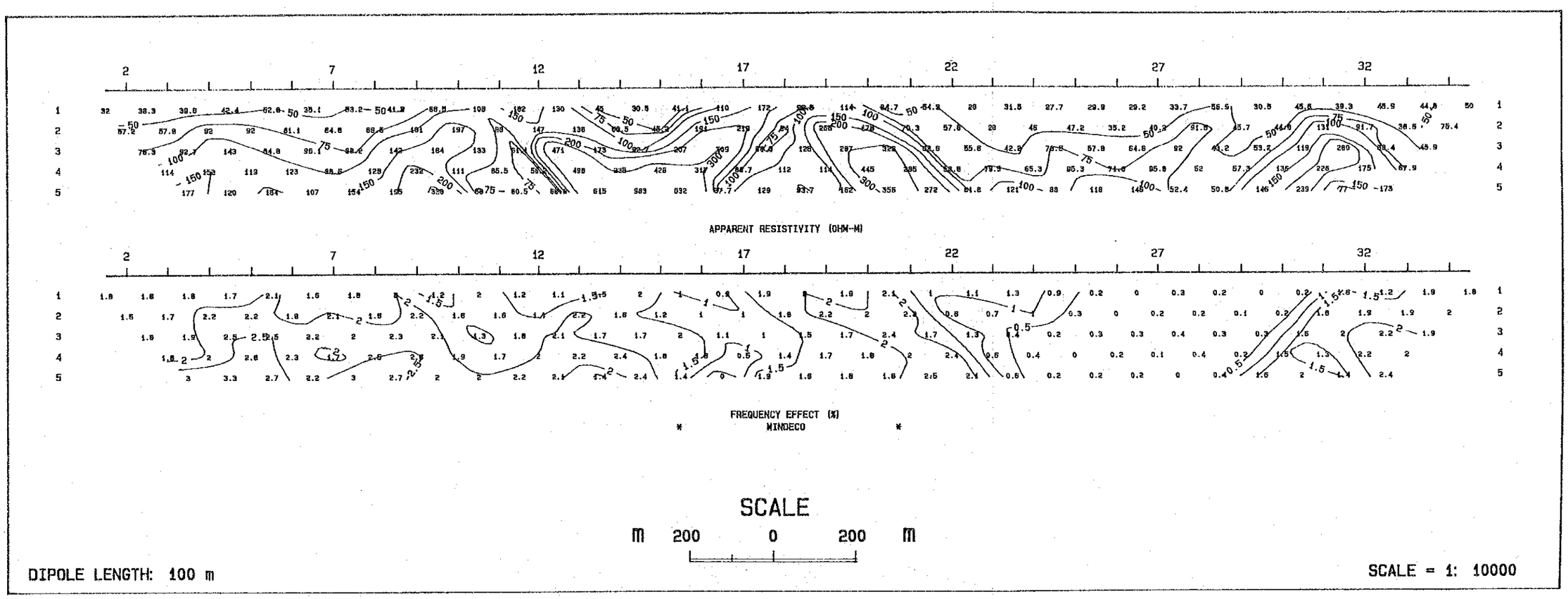

Fig. Ⅱ-11 Apparent Resistivity and PFE Pseudo Section (Line AK-1)

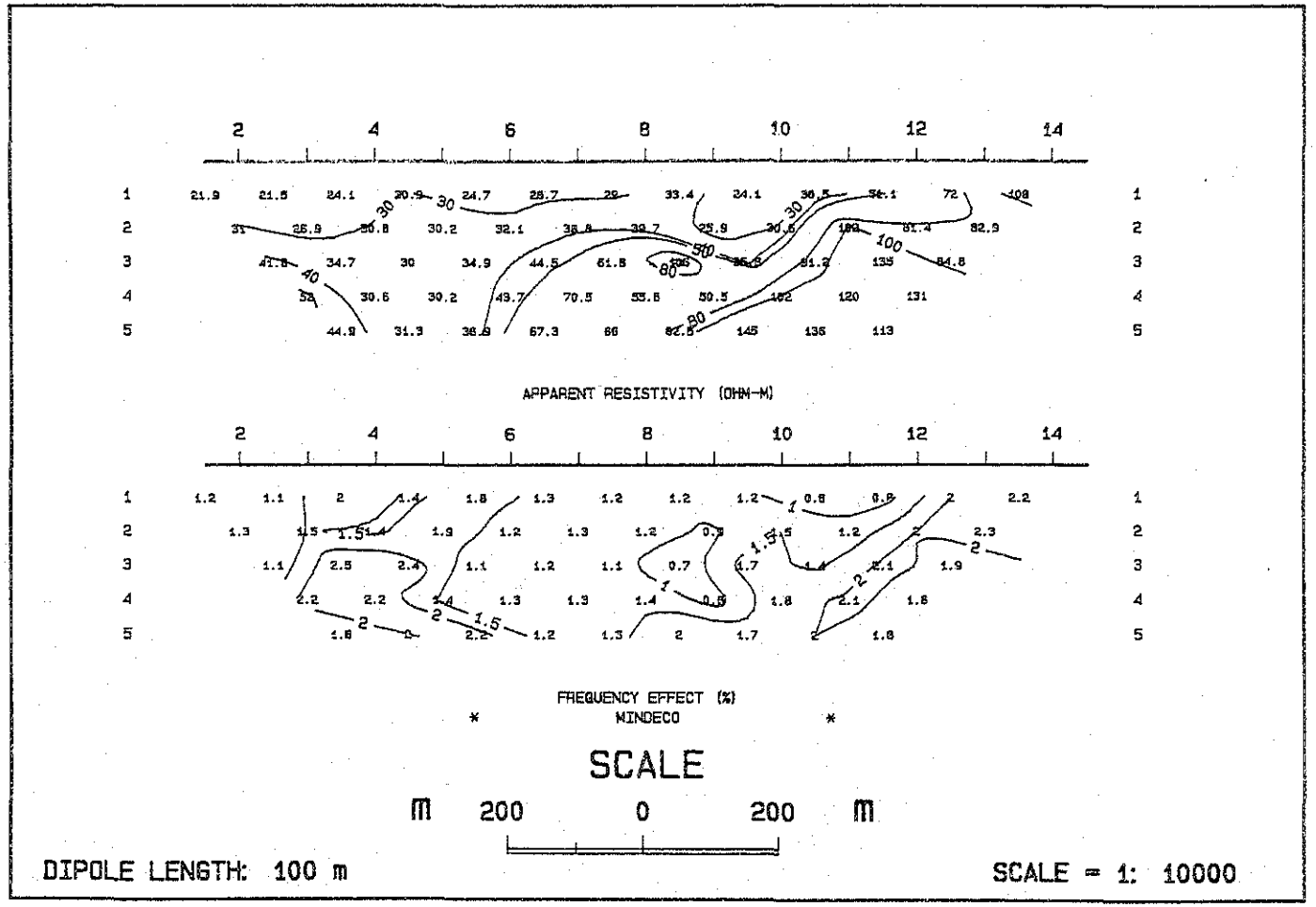

Fig. Ⅱ-12 Apparent Resistivity and PFE Pseudo Section (Line AK-2)

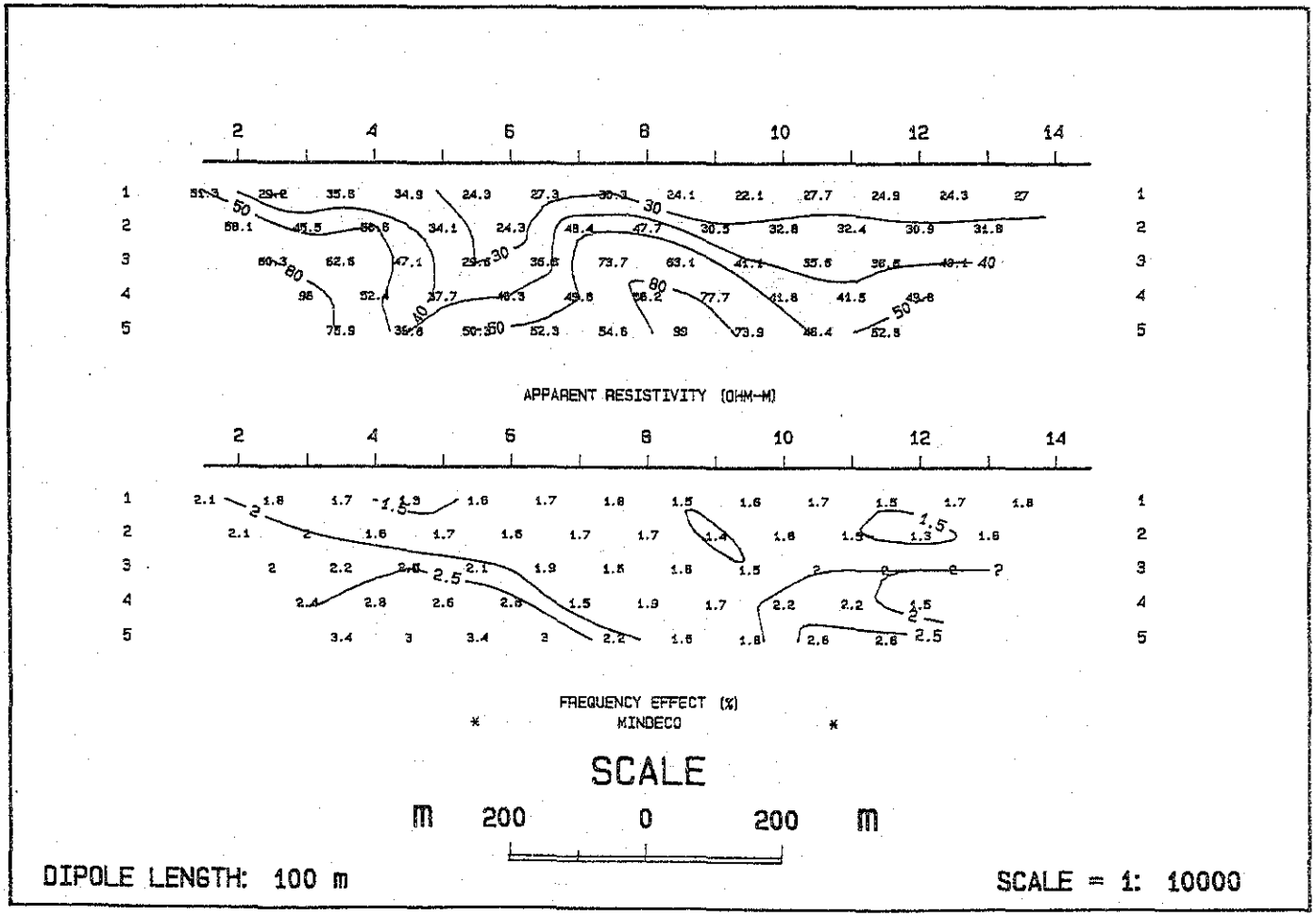

Fig. Ⅱ-13 Apparent Resistivity and PFE Pseudo Section (Line LM-1)

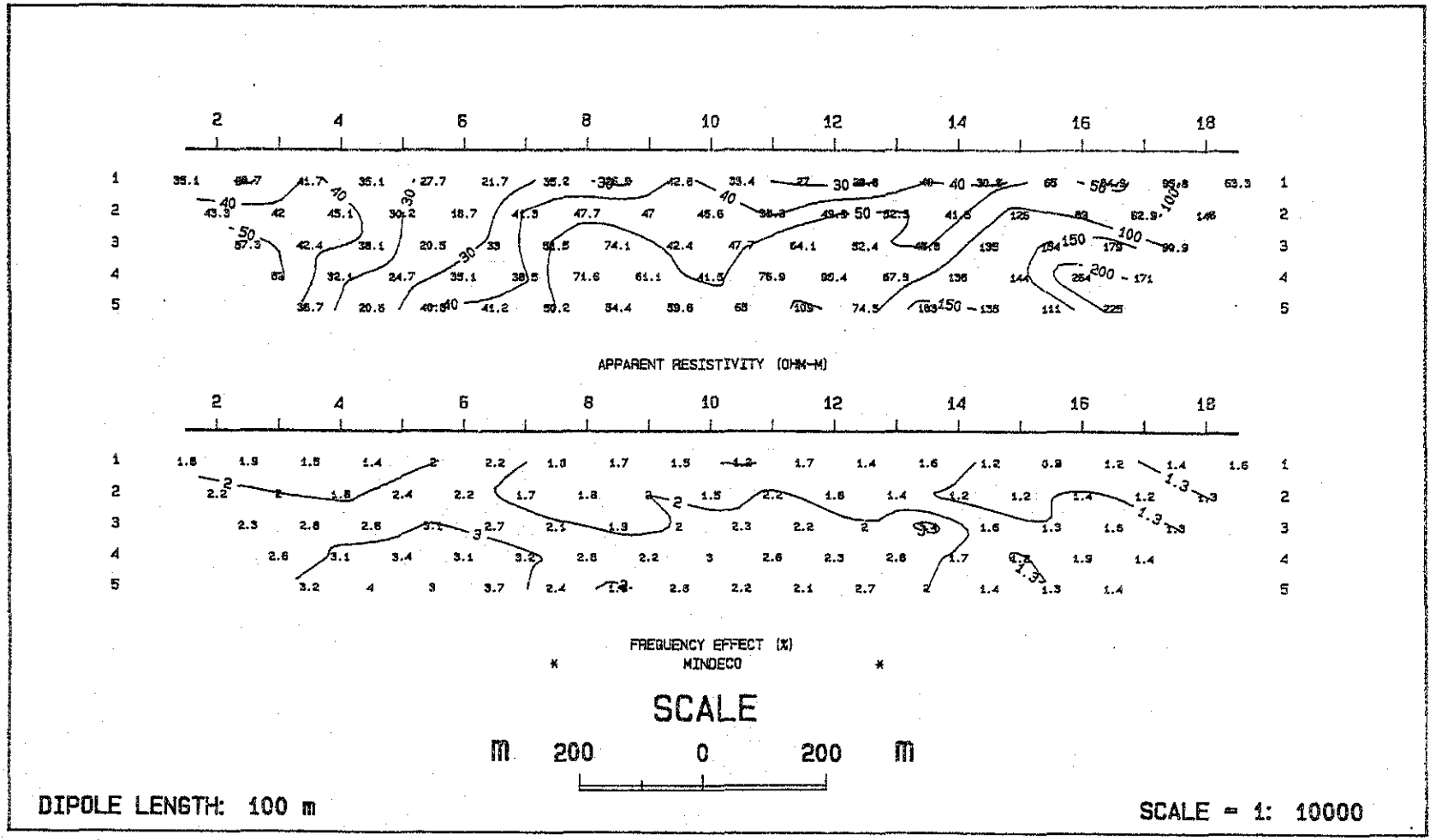

Fig. Ⅱ-14 Apparent Resistivity and PFE Pseudo Section (Line LM-2)

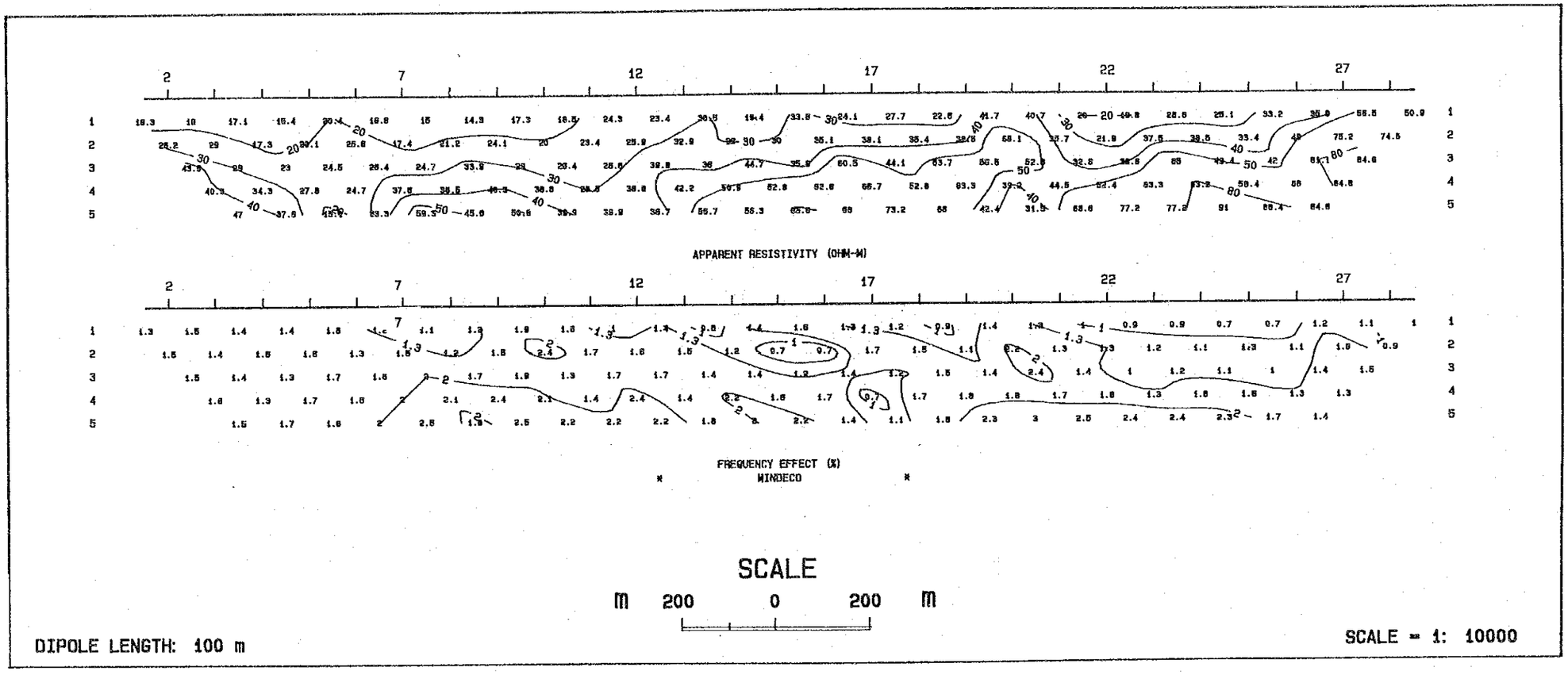

Fig. Ⅱ-15 Apparent Resistivity and PFE Pseudo Section (Line LM-3)

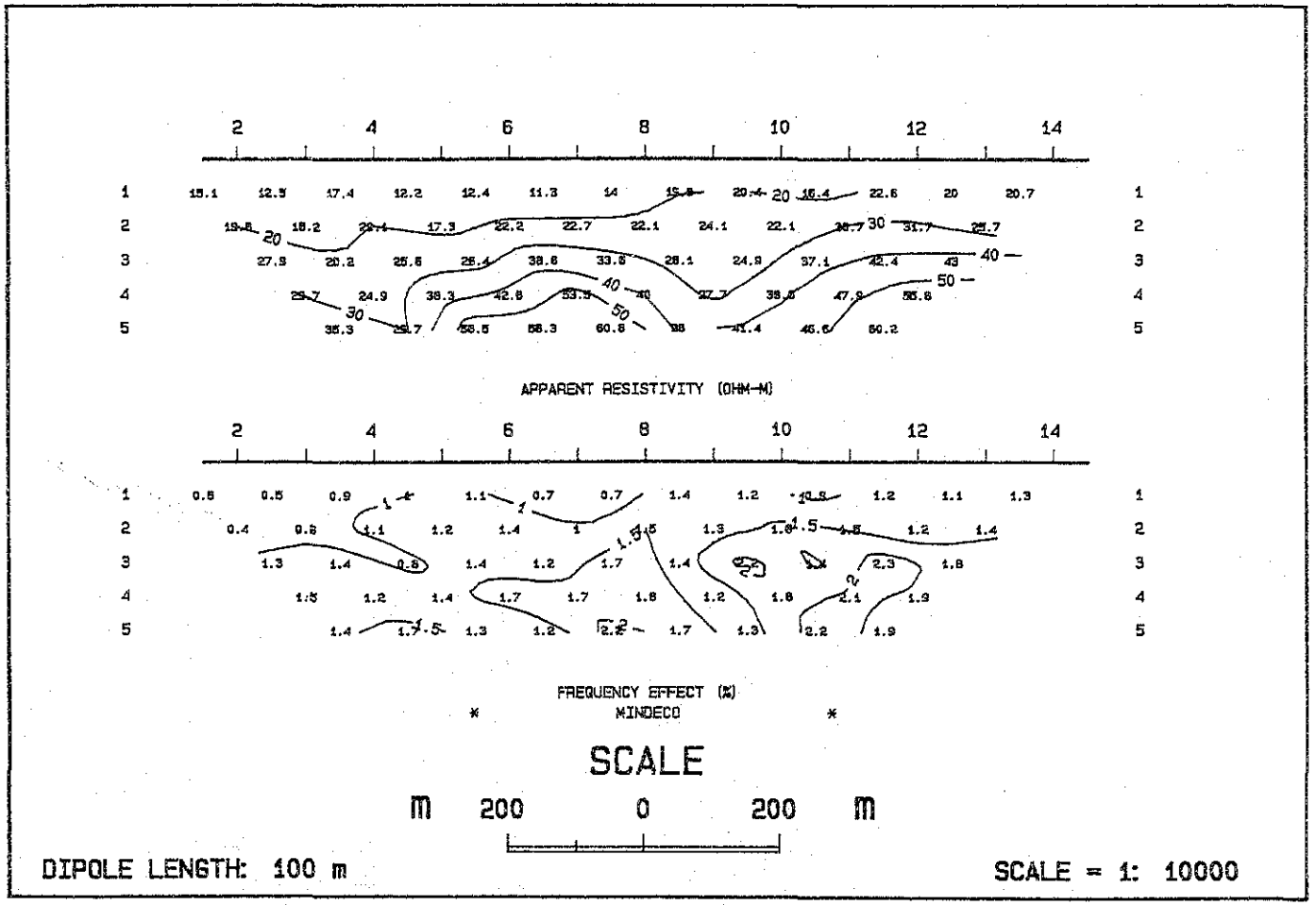

Fig. Ⅱ-16 Apparent Resistivity and PFE Pseudo Section (Line LM-4)

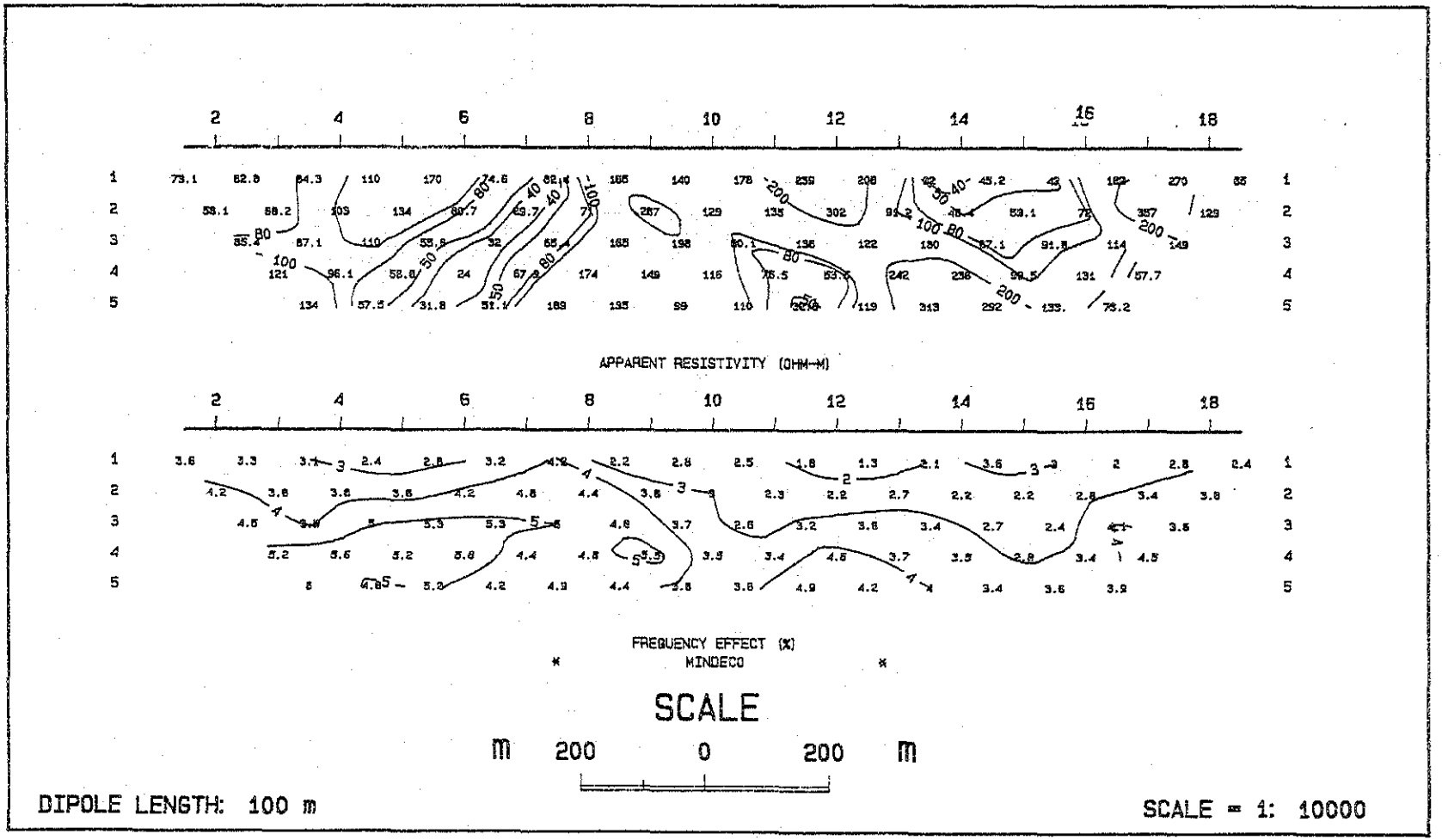

Fig. Ⅱ-17 Apparent Resistivity and PFE Pseudo Section (Line FZ-1)

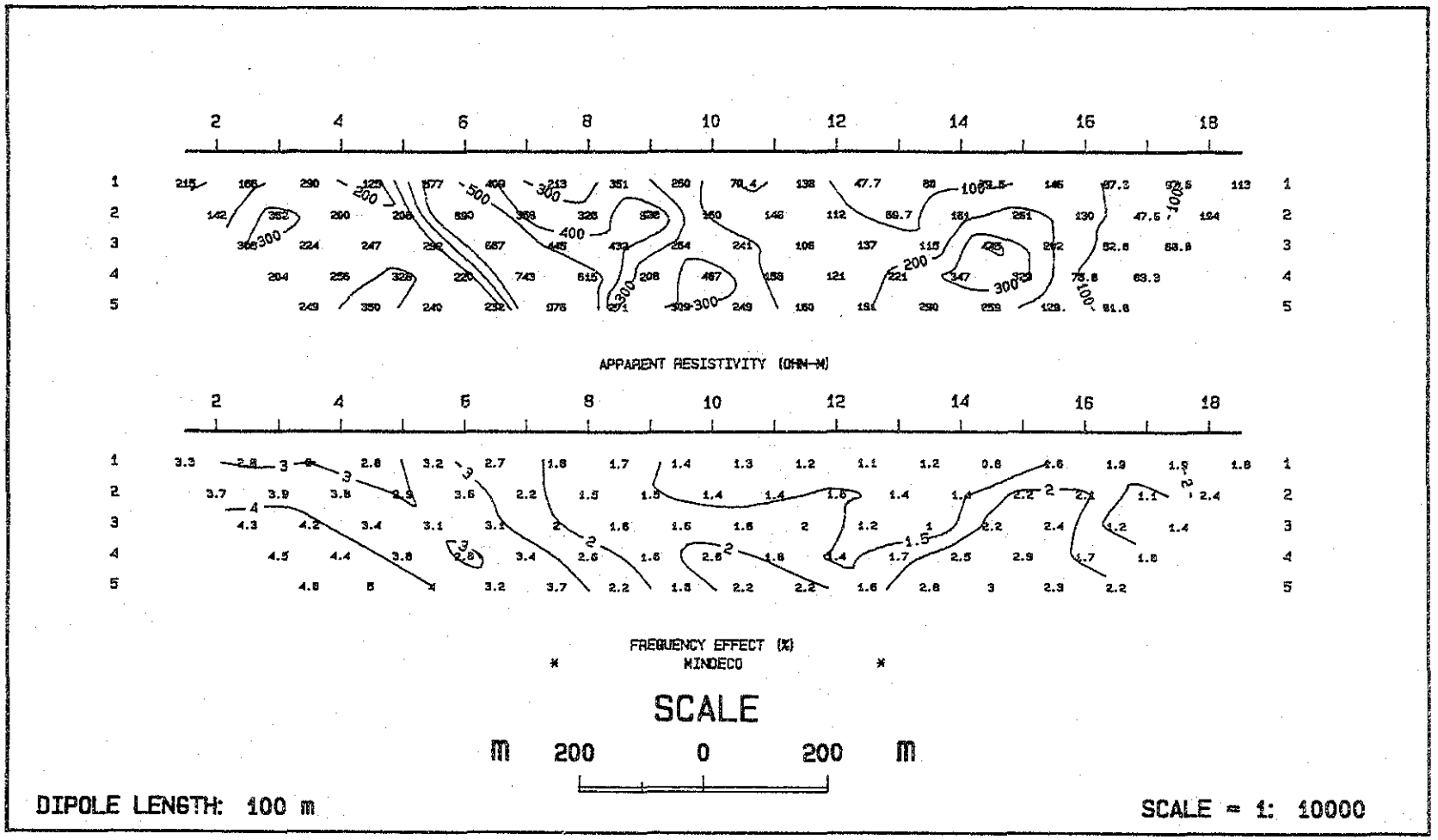

Fig. Ⅱ-18 Apparent Resistivity and PFE Pseudo Section (Line FZ-2)

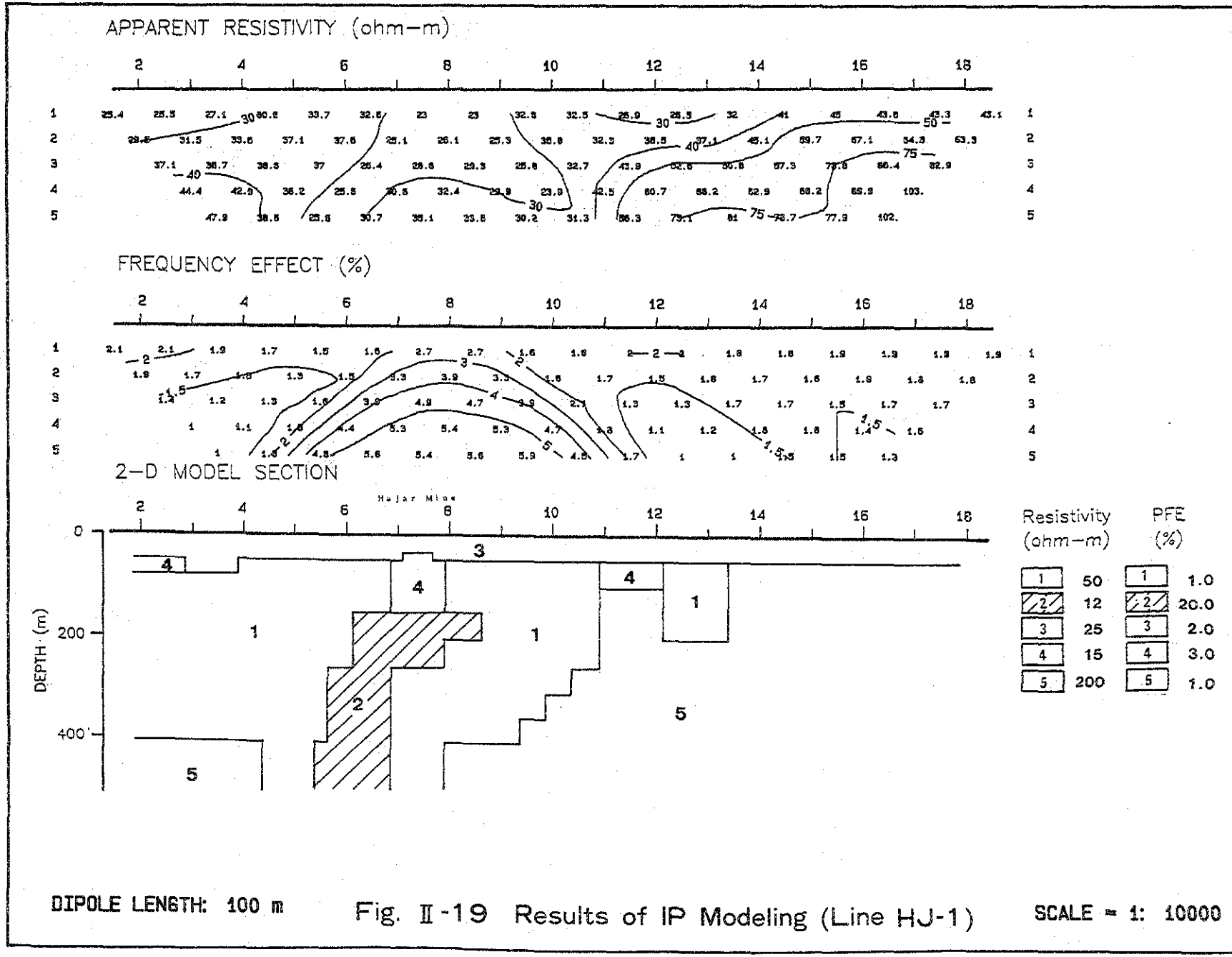

Fig. Ⅱ-19 Results of IP Modeling (Line HJ-1)

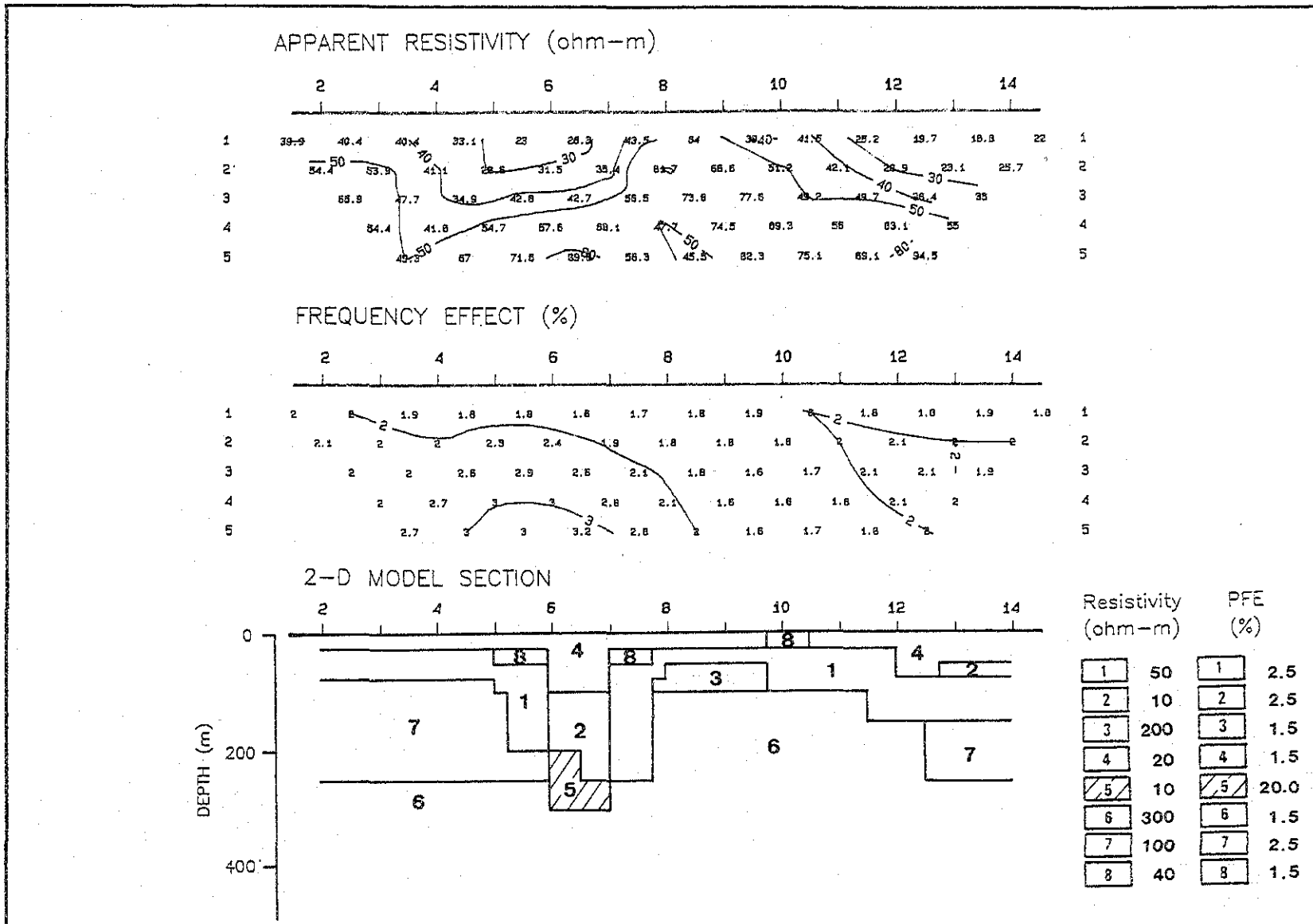

DIPOLE LENGTH: 100 m

Fig. Ⅱ-20 Results of IP Modeling (Line LM-1)

SCALE = 1: 10000

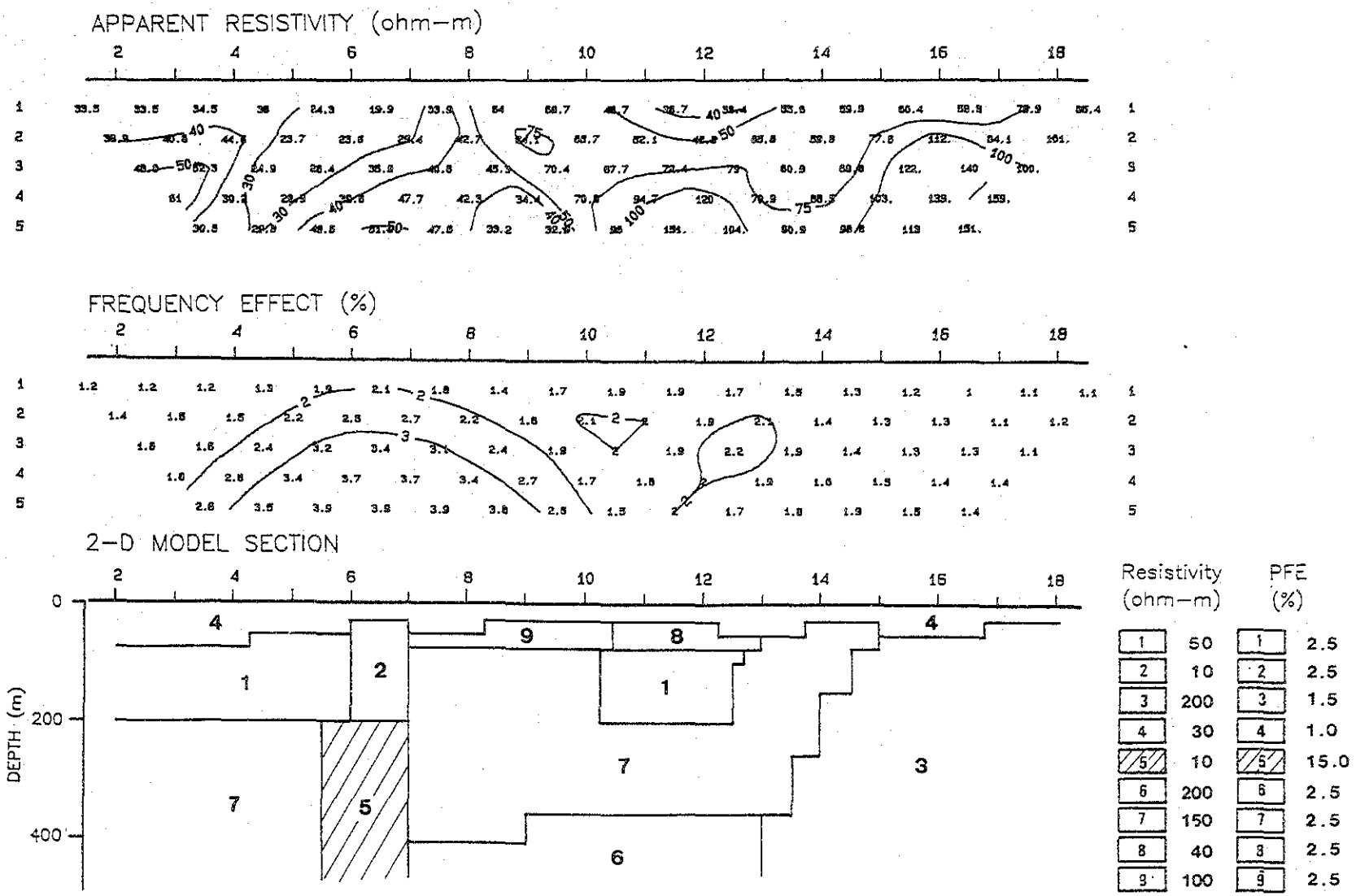

DIPOLE LENGTH: 100 m

Fig. II-21 Results of IP Modeling (Line LM-2)

SCALE = 1: 10000

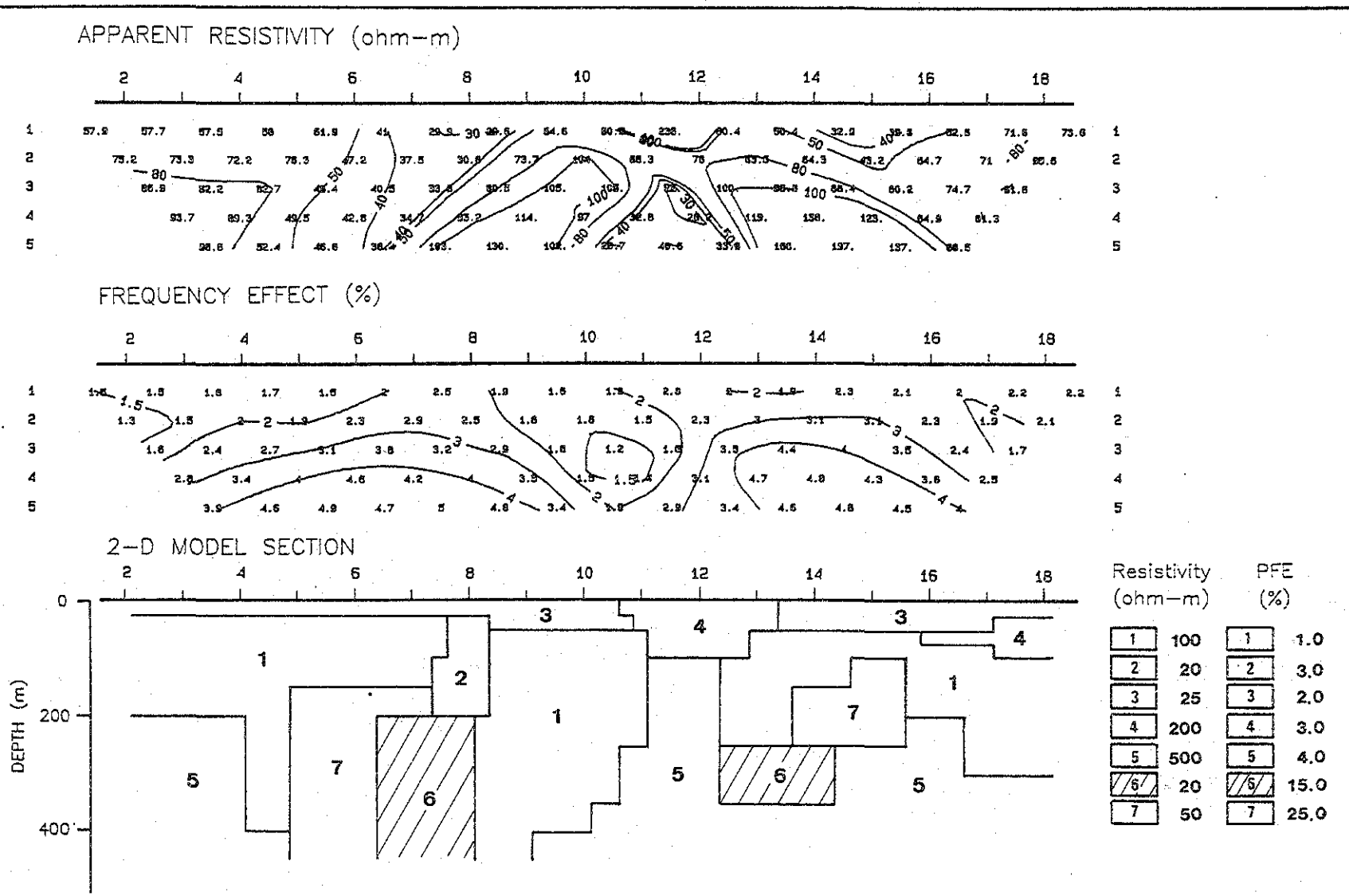

DIPOLE LENGTH: 100 m

Fig. Ⅱ-22 Results of IP Modeling (Line FZ-1)

SCALE = 1: 10000

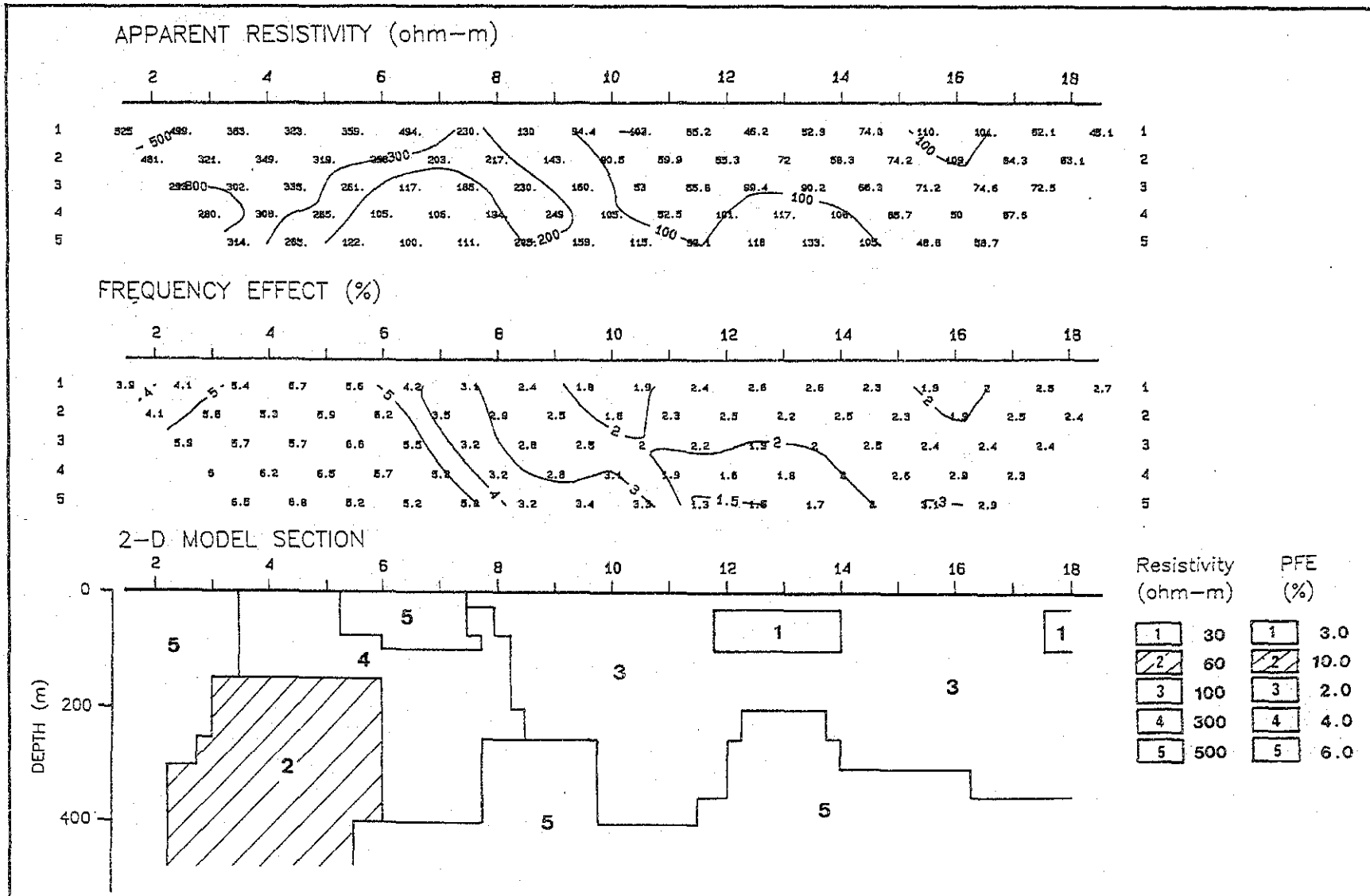

DIPOLE LENGTH: 100 m

Fig. Ⅱ-23 Results of IP Modeling (Line FZ-2)

SCALE = 1: 10000

COOPERATIVE MINERAL E 'LORATION
IN
HAOUZ CENTRAL AREA, .OROCCO
(PHASE II)

Fig II－24
GRAVITY CONTOUR MAP

(ρ=2.40g/cm³)

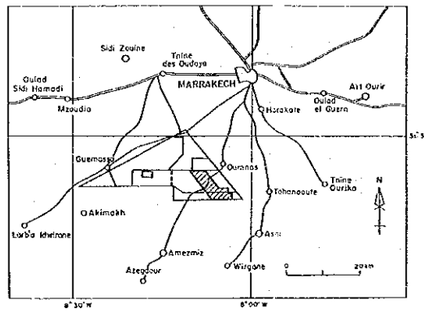

JAPAN INTERNATIONAL COOPERATION AGENCY
METAL MINING AGENCY OF JAPAN
FEBRUARY 1989
Prepored by MINDECO

0 2,500m

Scale 1 : 50,000

LEGEND

- ● HS－1 Boring Site
- ○ Gravity Station
- -40 / -45 Gravity Contour (milligal)
- (H) High Gravity Zone
- (L) Low Gravity Zone

COOPERATIVE MINERAL E PLORATION
IN
HAOUZ CENTRAL AREA, MOROCCO
(PHASE II)

Fig II – 25
GRAVITY CONTOUR MAP

(ρ=2.67g/cm³)

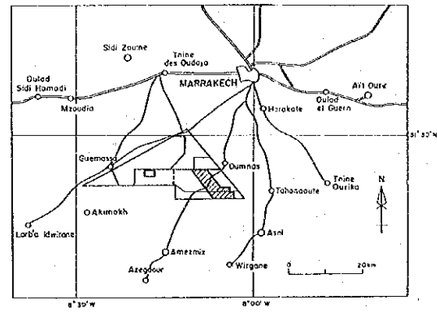

JAPAN INTERNATIONAL COOPERATION AGENCY
METAL MINING AGENCY OF JAPAN
FEBRUARY 1989

Prepared by MINDECO

0 2,500m

Scale 1 : 50,000

LEGEND

- ● HS – 1 Boring Site
- O Gravity Station
- -40 / -45 Gravity Contour (milligal)
- (H) High Gravity Zone
- (L) Low Gravity Zone

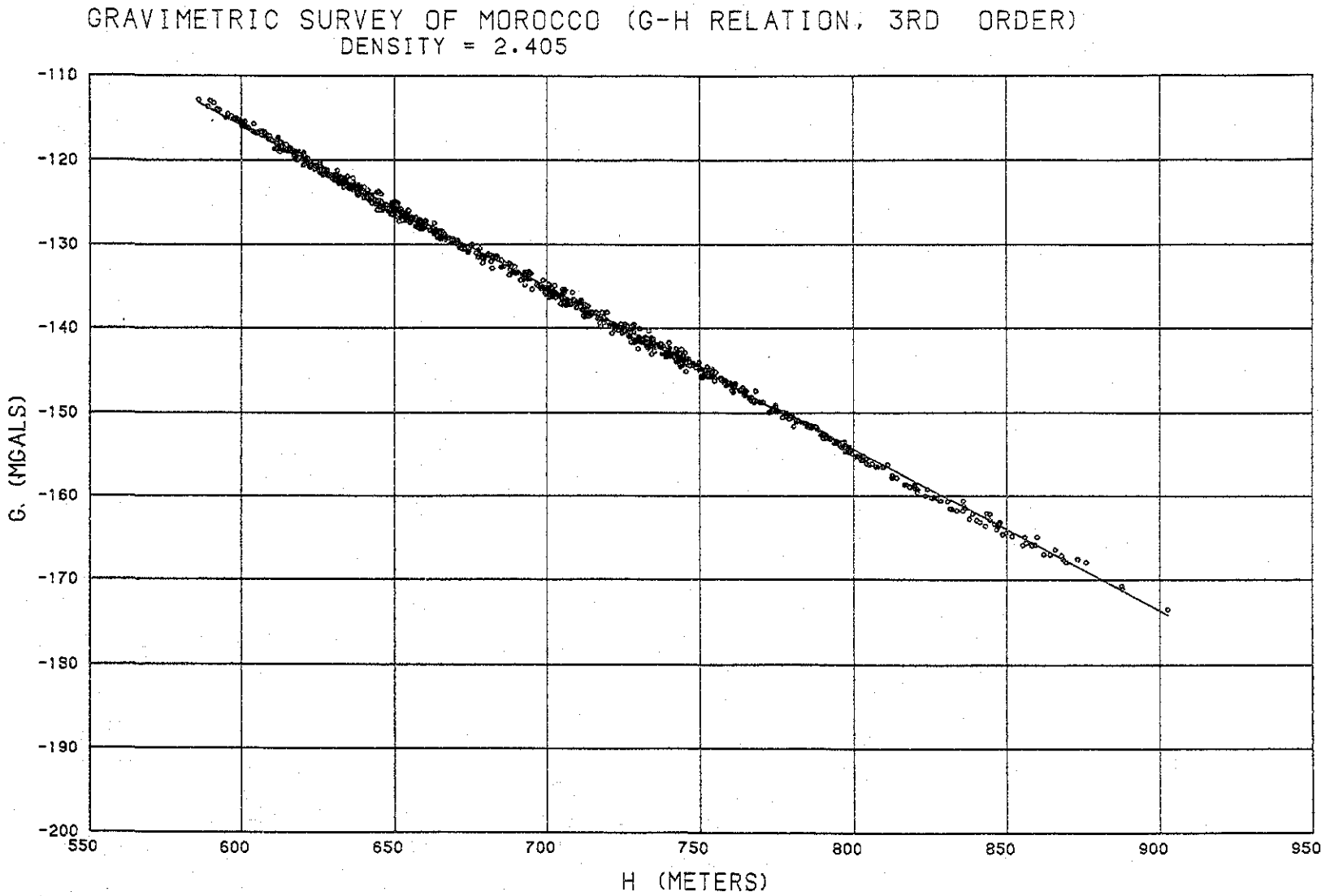

Fig. Ⅱ－26　Gravity versus Height Relation